Wind and Turbulence Effects on Raindrop Fall Speed

FIRAT Y. TESTIK^{a,b} AND ABDULLAH BOLEK^a

^a School of Civil and Environmental Engineering and Construction Management, University of Texas at San Antonio, San Antonio, Texas ^b Department of Mechanical Engineering, University of Texas at San Antonio, San Antonio, Texas

(Manuscript received 5 July 2022, in final form 6 December 2022)

ABSTRACT: Wind and turbulence effects on raindrop fall speeds were elucidated using field observations over a 2-yr time period. Motivations for this study include the recent observations of raindrop fall speed deviations from the terminal fall speed predictions (V_t) based upon laboratory studies and the utilizations of these predictions in various important meteorological and hydrological applications. Fall speed (V_f) and other characteristics of raindrops were observed using a high-speed optical disdrometer (HOD), and various rainfall and wind characteristics were observed using a 3D ultrasonic anemometer, a laser-type disdrometer, and rain gauges. A total of 26951 raindrops were observed during 17 different rainfall events, and of these observed raindrops, 18.5% had a subterminal fall speed (i.e., $0.85V_t \ge V_f$) and 9.5% had a superterminal fall speed (i.e., $1.15V_t \le V_f$). Our observations showed that distributions of sub- and superterminal raindrops in the raindrop size spectrum are distinct, and different physical processes are responsible for the occurrence of each. Vertical wind speed, wind shear, and turbulence were identified as the important factors, the latter two being the dominant ones, for the observed fall speed deviations. Turbulence and wind shear had competing effects on raindrop fall. Raindrops of different sizes showed different responses to turbulence, indicating multiscale interactions between raindrop fall and turbulence. With increasing turbulence levels, while the raindrops in the smaller end of the size spectrum showed fall speed enhancements, those in the larger end of the size spectrum showed fall speed reductions. The effect of wind shear was to enhance the raindrop fall speed toward a superterminal fall.

KEYWORDS: Turbulence; Rainfall; Wind; Drop size distribution

1. Introduction

Raindrop fall speed is an important parameter in rainfall microphysics characterizations for a range of applications. Examples of such applications include rainfall retrievals using weather radars, numerical hydrologic and climate modeling, soil erosion studies, and raindrop size distribution (DSD) calculations (e.g., Testik and Barros 2007; Testik and Gebremichael 2010). Over the past couple of decades, there have been several studies that reported notable deviations of in situ raindrop fall speed observations (V_f) from terminal raindrop fall speed (V_t) predictions based upon laboratory observations (see Fig. 4 of Testik et al. 2006; Montero-Martínez et al. 2009; Niu et al. 2010; Larsen et al. 2014; Montero-Martínez and García-García 2016; Bringi et al. 2018; Das et al. 2020; Chatterjee et al. 2022). Recently, Bolek and Testik (2022) observed significant raindrop fall speed deviations during a tornadic severe storm passage accompanied with major turbulence and wind speeds. There are significant implications of raindrop fall speed deviations from the predicted terminal values in the relevant applications such as rainfall modeling in weather and climate models, and rainfall retrieval using weather radars. For example, Pei et al. (2014) showed that raindrop fall speed deviations may induce large errors in rainfall retrievals using dual-polarization weather radars. Therefore, it is essential to elucidate the environmental conditions that cause raindrop fall speed deviations from predicted terminal values and the extent of these deviations. In this study, we investigated the effects of wind shear and turbulence on raindrop fall speeds through in situ raindrop observations using Testik and Rahman (2016). Raindrop observations in this study were collected at 10 m

a high-speed optical disdrometer (HOD) that was developed by

elevation as it is described later in section 2; hence, they were within the surface layer of the atmospheric boundary layer. The flow in the surface layer is almost always turbulent due to turbulence generation driven by the wind shear and buoyant convection (Kaimal and Finnigan 1994; Foken and Napo 2008; Nieuwstadt and Duynkerke 1996). This layer is populated by a wide range of eddy sizes, and hence, a wide range of velocity, time, and length scales corresponding to the largest (integral scale) to the smallest (Kolmogorov scale) scales, complicating the fall behavior of raindrops. Previous studies on flow turbulence effects on particle settling can be used to make inferences for the effects of turbulence on raindrops, given the nascency of the literature on the raindrop fall behavior under such conditions. One can expect that these scales have an important influence on the fall behavior of raindrops (Wang and Maxey 1993). In particular, one can expect that raindrop fall speeds would be influenced by the surface-layer turbulence when integral time scale τ_u is larger than the particle response time $[\tau_p$, see Eq. (8) later], and that the larger the raindrops (i.e., larger inertia), the larger the time scales are necessary to influence the raindrop fall behavior (e.g., Ayyalasomayajula et al. 2006; Rosa and Pozorski 2017; Tom and Bragg 2019). A governing parameter that accounts for the turbulent flow scale effects on the fall behavior of raindrops would be the Stokes number (St_n) , defined as $St_{\eta} = \tau_p/\tau_{\eta}$, where τ_{η} is the Kolmogorov time scale. As St_{η} value increases the particle is less affected by the small scales and the role of larger scales becomes more important. Raindrop response time τ_p calculated for the raindrop size spectrum is

Corresponding author: Firat Y. Testik, firat.testik@utsa.edu

between 0.2 and 0.8 s (Lovejoy and Schertzer 2008). Considering the τ_p range and the wide ranges of time scales of the turbulent flows in the surface layer (e.g., ranges of τ_u and τ_η values were 1.66-62.82 s and 0.004-0.225 s, respectively, during our field observations in this study), raindrops (and hydrometeors, in general) can be expected to have differing responses to turbulent flows. For example, for graupel in turbulent flows, Garrett and Yuter (2014) reported broadening of the distribution of the fall speed through both enhanced and reduced fall speeds as compared to predicted terminal speeds. In situ rainfall experiments reported both sub- (reduced) and superterminal (enhanced) raindrop fall speed observations (Testik et al. 2006; Montero-Martínez et al. 2009; Thurai et al. 2013; Larsen et al. 2014; Montero-Martínez and García-García 2016; Bringi et al. 2018; Bolek and Testik 2022). Various physical mechanisms, including preferential sweeping, loitering, nonlinear drag, and vortex trapping, may be responsible for the nonterminal raindrop fall speed observations in turbulent flows (Maxey 1987; Wang and Maxey 1993; Nielsen 1993; Fung 1993; Stout et al. 1995).

Maxey (1987) attributed the enhancement of particle fall speeds in turbulent flows to the preferential sweeping mechanism, which causes particle accumulation in the low-vorticity regions due to centrifuge effects. In the case of heavy particles in a turbulent carrier fluid under the action of gravity, such as raindrops in the air column, gravity-driven fall speeds of particles are enhanced by preferential sweeping of particles to the downward side of the eddies (e.g., Wang and Maxey 1993). It is not clear whether or not superterminal fall speed observations of raindrops, such as those observed by Montero-Martínez et al. (2009) and Larsen et al. (2014) for the raindrops in the smaller end of the size spectrum, can be attributed to the preferential sweeping mechanism. Nevertheless, it has been shown that preferential sweeping mechanism becomes effective at small scales, and when $St_{\eta} = O(1)$, it has a decreasing effect on the fall speed as St_η value increases (Maxey 1987; Wang and Maxey 1993; Aliseda et al. 2002; Good et al. 2014). Ireland et al. (2016) discussed that, under the action of gravity, particle interaction time with ambient turbulence is reduced and particles may be distributed more uniformly, meaning the degree of preferential sampling decreases. As such, Froude number (Fr = a_n/g ; where a_n is Kolmogorov acceleration scale and g is gravitational acceleration), which provides an indication of the relative roles of turbulence and gravity, becomes another important parameter for raindrop fall in atmospheric turbulence. Investigating the multiscale nature of preferential sweeping, Tom and Bragg (2019) showed that particles with $St_{\eta} \ge O(1)$ and $Fr \ll 1$ may also experience enhanced settling speeds through preferential sampling mechanism. Furthermore, they showed that the relevant flow scales increase with an increase in St_n and particles preferentially sample at scales larger than the dissipation scales. In the light of these findings and considering that all of the observed raindrops in our study had $St_{\eta} \ge O(1)$ and Fr values ranging from 0.004 to 1.7, preferential sweeping mechanism may have been effective for some of the superterminal raindrops observed in our study.

Reduced particle fall speeds in turbulent flows have been reported in various studies (Murray 1970; Nielsen 1993; Fung 1993; Stout et al. 1995; Yang and Shy 2003; Kawanisi and

Shiozaki 2008; Good et al. 2014; Rosa and Pozorski 2017; Ren et al. 2020). Within the context of rainfall, several studies reported subterminal fall of raindrops (Testik et al. 2006; Montero-Martínez et al. 2009; Thurai et al. 2013; Montero-Martínez and García-García 2016; Bringi et al. 2018; Bolek and Testik 2022). Plausible causes for the reduced particle fall/settling speeds may be nonlinear drag effects, loitering, and/or vortex trapping (Nielsen 1993). For larger particles, such as raindrops with diameters ranging approximately from 0.1 to 6-8 mm, nonlinear drag formulations, rather than Stokes drag law, represent the drag forces acting on particles more adequately. Nonlinearity of drag force on particles results in reduced particle settling speeds in turbulent flows, and reductions in particle settling speeds become larger as the particle Reynolds number [Re_n; defined later in Eq. (10)], hence particle size, increases (Stout et al. 1995; Fung 1998; Good et al. 2014). Particles experiencing fluid flow in the opposite direction of the fall direction and particles trapped by horizontally moving vortices may experience the loitering and vortextrapping mechanisms, respectively, that cause particle settling speed reductions (Nielsen 1993). Nevertheless, it is not likely that vortex-trapping mechanism would cause fall speed deviations of raindrops from predicted terminal speeds as heavy inertial particles, such as raindrops, can spiral out from the vortices due to their inertia (Maxey and Corrsin 1986; Chen et al. 2020). Therefore, nonlinear drag effects and loitering may be considered as two potential mechanisms that are responsible for the subterminal raindrop observations.

In this study, we aimed to link sub- and superterminal fall speed observations with turbulence and wind shear and elucidate the underlying physical mechanisms through rainfall and wind observations over an approximately 2-yr period. Section 2 describes our field site and data collection methodologies, and section 3 provides a background for our wind and turbulence analyses. Section 4 presents our results with subsections discussing vertical wind effects (section 4a), turbulence effects (section 4b), and wind shear effects (section 4c) on raindrop fall. Section 5 provides a summary and conclusions of our study. Note that nomenclature section is provided as an appendix to this article while also providing symbol definitions throughout the text for the readers' convenience.

2. Field site and data collection

In situ rainfall observations were conducted at our outdoor rainfall laboratory located at the West Campus of the University of Texas at San Antonio (coordinates: 29°34′43.37″N, 98°37′49.90″W; elevation: 296 m above mean sea level). Satellite images of our field site and the surrounding area are presented in Fig. 1. The field site is located at the outskirts of the city with sparsely distributed low-rise buildings on a flat, nonsloping (<4% land slope) terrain. The average building height within 1 km radius of the site is approximately 15 m with a maximum building height of 28 m at 820 m east of the field site. As can be seen in the figure, small vegetation and trees shorter than 5 m in height surround the field site.

The field site is equipped with a camper trailer for dry working space during precipitation events, a customized 10-m-tall

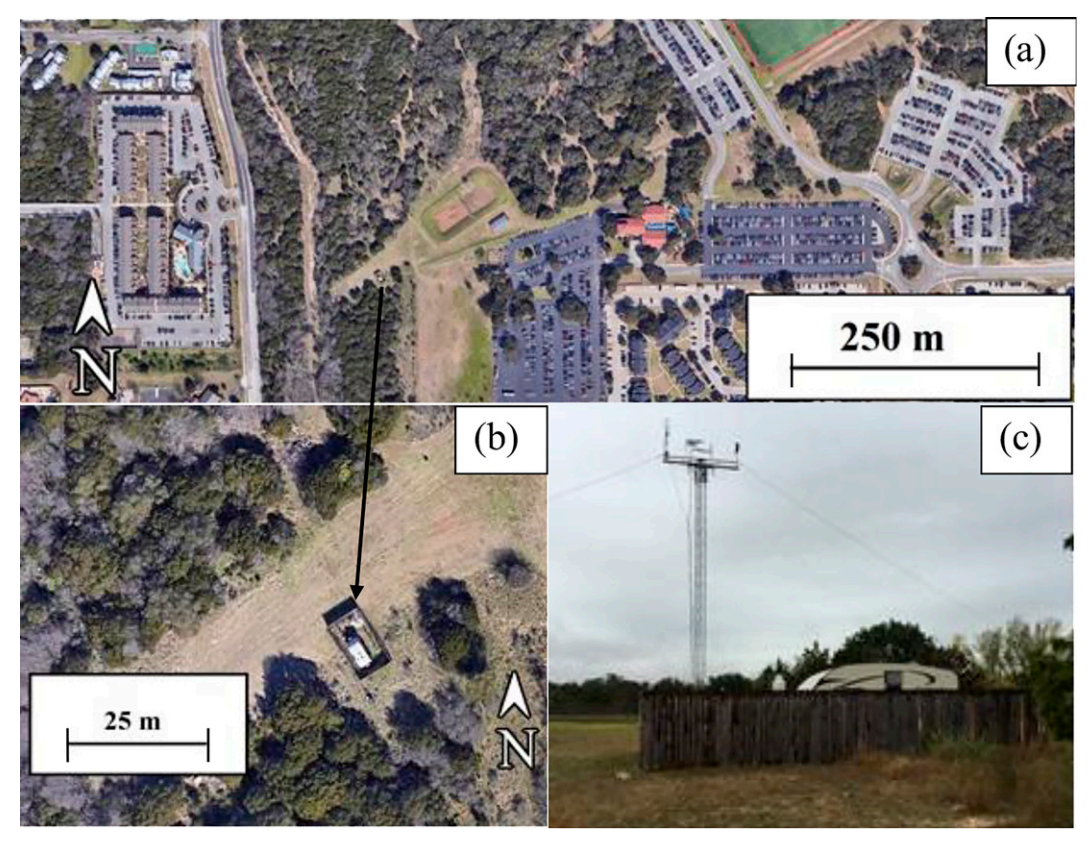


FIG. 1. Images showing the field site and the surrounding landscape and infrastructure: (a),(b) satellite images at different zooming levels, and (c) a photograph of the field site that shows HOD and wind anemometer installations at the top of the 10-m-high tower.

instrumentation tower, and various standard meteorological instrumentations such as rain gauges, anemometers, and disdrometers. For this study, the two critical instrumentations were HOD for raindrop observations (Testik and Rahman 2016) and a commercial 3D ultrasonic anemometer (R. M. Young 81000) for wind measurements. HOD is ideally suited for accurate raindrop fall speed measurements (see, e.g., Rahman and Testik 2020). The details of the HOD and a thorough validation of its measurement capabilities can be found in Testik and Rahman (2016). Briefly, HOD includes a high-speed camera that points at an LED light and captures the side-view (i.e., orthogonal to the gravity direction) silhouettes of hydrometeors at a specified rate (1000 frames per second in this study). A sensing unit triggers HOD when hydrometeors are present within the virtual measurement volume of 24 500 mm³ $(H \times W \times L: 70 \text{ mm} \times 5 \text{ mm} \times 70 \text{ mm})$ around the camera's focal plane. When triggered, HOD captures a predefined number of high-quality (1024 pixels × 1024 pixels) sequential hydrometeor images (10 images per raindrop in this study). The HOD's postprocessing software then analyzes the sequential images for all of the captured hydrometeors using image processing techniques and algorithms. In the analysis, the software identifies the hydrometeor boundaries, and then calculates a number of geometric (e.g., D) and dynamic characteristics (e.g., V_f). Multiple observations of the same hydrometeor

through sequential high-speed images enable calculations of the hydrometeor characteristics at multiple instances. In this study, instantaneous measurements for a given raindrop were averaged to reduce the scatter of the calculated instantaneous values induced by transient processes (e.g., raindrop oscillations) and measurement errors (e.g., optical distortion). Testik and Rahman (2016) showed that maximum errors in HOD's instantaneous diameter measurements are about 11% for drops that are 0.5 mm in diameter and decrease with increasing raindrop size, becoming less than $\sim 3\%$ for raindrops that are 5 mm in diameter and larger. In this study, HOD measurements for only raindrops that are larger than 0.75 mm in diameter (a total of 26951 raindrops) are reported and the maximum error in diameter measurements is confined to less than 10%. Since the uncertainty of the HOD measurements of both D and V_f is less than 10% for raindrops with D > 0.75 mm, here, raindrops with fall speeds that are 15% faster than the corresponding predicted terminal speeds are classified as superterminal raindrops and those that are 15% slower than the corresponding predicted terminal speeds are classified as subterminal raindrops. The 3D ultrasonic anemometer used in this study can measure wind velocity up to 40 m s⁻¹ with 0.01 m s⁻¹ resolution and an accuracy of $\pm 1\%$ between 0 and 30 m s⁻¹ wind speeds and $\pm 3\%$ between 30 and 40 m s⁻¹ wind speeds. OTT Parsivel² disdrometer and OTT Pluvio² rain gauge, which were mounted

TABLE 1. Rainfall events considered in this study with a summary of relevant rainfall and raindrop characteristics. Table columns are event No. = event number; date = event date; start and end = event start and end time, respectively; TRA = total rain amount measured by $Pluvio^2$; $\overline{R} = average$ rainfall rate measured by $Pluvio^2$; max(R) = maximum rainfall rate measured by $Pluvio^2$; N = total number of raindrops; sub- and super = subterminal and superterminal raindrop percentages, respectively.

Event No.	Date	Start (UTC)	End (UTC)	TRA (mm)	\overline{R} (mm h ⁻¹)	$\max(R)$ (mm h^{-1})	N	Sub (%)	Super (%)
1	3 May 2019	0751	1145	34.2	8.77	138.6	1557	20.1	5.8
2	4 May 2019	0104	0304	30	15	89.7	1720	16.8	9.7
3	4 Jun 2019	1956	2218	4.59	1.94	4.8	689	3.5	0.0
4	10 Jun 2019	0229	0451	9.9	4.3	25.7	602	4.5	2.7
5	17 Jun 2019	0515	0652	26.9	18	123.9	785	14.1	3.6
6	24 Jun 2019	1824	2041	30.4	13.5	53.5	1368	17.5	15.9
7	11 Sep 2019	2028	2227	3.6	1.8	11.5	882	4.5	1.5
8	19 Sep 2019	0144	0342	26.1	13.1	135.1	919	18.8	18.9
9	16 Oct 2019	0111	0253	8.8	5.25	45.7	700	11.1	2.9
10	16 Oct 2019	0650	1205	12.1	2.3	6.3	1969	13.5	5.1
11 ^a	24 Oct 2019	2323	0656	92.7	12.4	142.1	3970	28.0	19.0
12	16 May 2020	0320	0740	32.3	5.7	74.8	2678	22.0	8.7
13	25 May 2020	0010	0615	43.7	7.3	109.3	3188	17.0	6.9
14	28 May 2020	2150	2359	17.8	8.9	85.2	567	33.2	20.1
15	4 Sep 2020	1810	2130	4.7	1.4	14.2	793	7.8	4.7
16	10 Sep 2020	0500	0840	17.9	4.88	56.4	1473	31.2	11.9
17	28 Nov 2020	1400	2223	21.8	2.6	30.5	3091	14.9	6.1

^a Event continued until 0656 UTC on the following day (25 Oct 2019).

on top of 2 m height poles, were used to obtain the rainfall parameters such as total rain accumulation (TRA) and rainfall rate (R).

The HOD and 3D ultrasonic anemometer were mounted on top of a 10 m tower, and they were mounted such that their measurements were not in the wake of the tower. The ultrasonic anemometer collected three-dimensional wind velocity data at 32 Hz continuously. Orientation of the ultrasonic anemometer was set such that the positive horizontal coordinates were from north to south and from east to west, and the positive vertical coordinate was against the direction of gravity. The anemometer and HOD were synchronized through a data acquisition software using LabVIEW to be able to identify the wind velocity information corresponding to each of the raindrops monitored by the HOD within 31.25 ms of the data collection time.

In this study, in situ measurements were conducted during 17 independent rainfall events that occurred between May 2019 and November 2020. There were no specific criteria in terms of meteorological and environmental factors (e.g., rain rate, wind speed, and temperature) for selecting these 17 rainfall events for observations during this approximately 1.5-yr period. Here, rainfall event is defined as a period of continuous rain accumulation of at least 1 mm, and separated from the next rainfall event by a dry period of at least 1 h. Table 1 lists the rainfall events considered in this study with information on the date and time of the events, rainfall amounts and rates, observed number of raindrops, and sub- and superterminal raindrop percentages. As can be seen in Table 1, percentages of subterminal raindrops were higher than the percentages of superterminal raindrops for almost all of the events. The physical processes responsible for the sub- and superterminal raindrop occurrences were detailed later in this

article. Note that average rainfall rate \overline{R} for an event was calculated by dividing the total rain amount, TRA, measured by Pluvio² to the event duration for a given rainfall event.

3. Wind and turbulence analysis

Ensemble statistics are not possible for the analysis of in situ wind velocity measurements. Therefore, temporal statistics of the measured wind velocity time series were used to represent the ensemble statistics using the ergodicity and stationarity hypotheses (e.g., Katul et al. 1994). This approach has been commonly practiced for atmospheric boundary layers (e.g., Oncley et al. 1996; Higgins et al. 2013). For this practice, the averaging duration within the limited length of the data series must be sufficiently long to include a large number of independent realizations of the sampled flow velocities. This requires adequate selection of the time series length for time averaging of the variable of interest. The adequate length of the time series for calculating the moments of a single variable and covariance of two variables are different. In general, the adequate time series length can be achieved by selecting an averaging time that is much larger than the integral time scale of the series (Lenschow et al. 1994). Here, 5-min duration was used in calculating all of the turbulence quantities which is much larger than the maximum integral time scale, 62.82 s, of the data that we collected throughout this study. The 5-min-long subdatasets to calculate the wind and turbulence characteristics for each raindrop were obtained from the event-long anemometer data for the time period between the instant that the raindrop was captured by the HOD and 5 min prior to that instant. Ideally, a shorter duration would be preferable to observe the turbulence and raindrop interrelations during typical rainfall events with

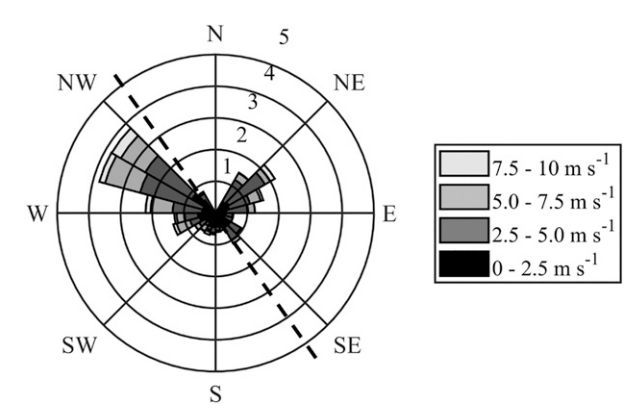


FIG. 2. Wind rose that presents measured mean wind direction and speed for the entire rainfall events. Bin widths for wind direction is 15° and for wind speed is 2.5 m s⁻¹. Directions are shown on the wind rose and color mapping for the speed is shown in the legend. Circles represent the number of 5-min wind subdatasets to indicate the duration. From inner to outer circle, the number of subdatasets corresponding to each circle increases from 1000 to 5000 with increments of 1000. The dashed line presents the orientation of the HOD's axis.

rapid changes in turbulence quantities. Nevertheless, shorter durations lead to increased errors in calculations of turbulence quantities, and the duration of 5 min has been typically used in relevant turbulence calculations (e.g., Nemes et al. 2017; Garrett and Yuter 2014).

For the anemometer wind velocity measurements, the spike removal procedure by Vickers and Mahrt (1997) was applied before any statistical and turbulence parameter calculations. This was necessary because raindrops can cause spikes when they accumulate on the anemometer's transducer face. Moreover, the subdatasets with total number of spikes more than 1% of the total subdataset points (9600 data points per 5-minlong subdatasets) was not used in the analysis (Vickers and Mahrt 1997). To align the horizontal wind velocity components in the streamwise direction and reduce the terrain slope effects on the vertical wind velocity component, the double rotation procedure was employed (Wilczak et al. 2001). A combined wind rose that provides the wind speed and horizontal wind direction information for all of the 17 rainfall events considered in this study is provided in Fig. 2. As can be seen from the wind rose, horizontal wind directions were mainly from around northwest-west and northeast directions, and the 5-min-averaged horizontal speeds were as fast as approximately 10 m s⁻¹. Streamwise, lateral, and vertical wind velocity components are denoted as u, v, and w, respectively. For each 5-min subdatasets, mean velocity components at a given instant $(\overline{u}, \overline{v}, \overline{w}$ —means of u, v, w components, respectively) were calculated using simple moving averaging (SMA) with a window length of 240 s. Adequacy of the selected time window length was verified by confirming that the average vertical wind speeds for this window length were close to zero as one would expect due to turbulent motions. Fluctuations of the velocity components [u'(t), v'(t), and w'(t)]—fluctuations of u, v, and w components, respectively] were calculated using

the measured velocity component at a given time t and the mean of the relevant velocity component calculated using SMA by Reynolds decomposition [e.g., $u'(t) = u(t) - \overline{u}$]. The turbulent kinetic energy (k) values for the subdatasets were calculated by using the three components of the velocity fluctuations as follows:

$$k = 0.5(\overline{u'^2} + \overline{v'^2} + \overline{w'^2}). \tag{1}$$

Here, overbar denotes temporal averaging. The integral time (τ_u) and length (l_u) scales were calculated by considering only the streamwise velocity component as follows:

$$\tau_u = \int_0^\infty \rho_u(T)dT, \quad l_u = \tau_u \overline{u}. \tag{2}$$

Here, $\rho_u(T)$ is the <u>autocorrelation</u> coefficient defined as $\rho_u(T) = \overline{u'(t)u'(t+T)}/u'(t)^2$, and *T* is time lag.

Turbulent kinetic energy dissipation rate (ε) values used in this study were calculated using the second-order structure function method ($\varepsilon_{\text{SSFM}}$) (e.g., Albertson et al. 1997; Davidson 2015; Muñoz-Esparza et al. 2018; Bolek and Testik 2022). It is well-known that ε values calculated using different methods may be significantly different (e.g., Jabbari et al. 2016; Muñoz-Esparza et al. 2018). Therefore, calculated ε_{SSFM} values were compared with ε values calculated using another commonly used method for sonic anemometer measurements called the inertial dissipation method (ε_{IDM}) (e.g., Oncley et al. 1996; Piper and Lundquist 2004; Chamecki and Dias 2004). Both of these methods for ε calculations are based on Kolmogorov's second similarity hypothesis that relates ε and velocity difference between two points in the inertial range of three-dimensional isotropic turbulence, and these methods can be implemented using one-point measurements of velocity time series and Taylor's frozen turbulence hypothesis (e.g., Muñoz-Esparza et al. 2018). The $\varepsilon_{\rm SSFM}$ calculations were conducted as follows. The $\varepsilon_{\rm SSFM}$ values were computed in the temporal space through Taylor's frozen turbulence hypothesis using Eq. (3) below. Taylor's hypothesis is applicable when the ratio of the root-mean-square (rms) velocity to the mean velocity is smaller than 0.1 ($\sigma_u/\overline{u} < 0.1$ for the streamwise velocity component) (Piper and Lundquist 2004). In this study, the average σ_u/\overline{u} of all events was found as 0.399. Although this average value is larger than 0.1, it is smaller than 0.49 that was found by Katul et al. (1994) to assume the validity of Taylor's hypothesis for the inertial range:

$$\varepsilon_{\rm SSFM} = \frac{1}{\overline{u}\zeta} \left[\frac{D_u(\zeta)}{C_k} \right]^{1.5}.$$
 (3)

Here, $D_u(\zeta) = \overline{[u'(x+\zeta) - u'(x)]^2}$ is the streamwise second-order structure function with the time separation of ζ , and $C_k \approx 2.0$ is the Kolmogorov constant. In this study, the range of ζ was chosen as 0.1–2 s for the computations since the structure function and Kolmogorov's inertial range slope (in time domain, $\zeta^{2/3}$) was in a good agreement for this ζ range, and also this range was used in previous studies (Muñoz-Esparza et al. 2018; Bodini et al. 2018, 2019). The $\varepsilon_{\rm IDM}$ calculations were

conducted as follows. First, the streamwise velocity was low-pass filtered with a cutoff frequency of 4 Hz where the Nyquist frequency was 16 Hz. Then, 1D turbulent energy spectra for the streamwise velocity component [S_u , see Eq. (4)] were computed with 2^{12} discrete Fourier transform points. In atmospheric surface layers, the spectra are given in a normalized form for different field site characteristics, including terrain features and roughness elements (Tieleman 1992a; Teunissen 1980; Kaimal and Finnigan 1994; Højstrup 1981). The 1D turbulent energy spectra for neutral surface layers are defined as in Eqs. (4) and (5):

$$S_u(n) = \frac{1}{\pi} \int_0^\infty e^{-i\pi n} R_u(\tau) d\tau, \tag{4}$$

$$\frac{nS_u(n)}{u_*^2} = \frac{Af^{\gamma}}{(C + Bf^{\delta})^{\beta}}.$$
 (5)

Here, $S_u(n)$ is the 1D turbulent energy spectra, $R_u(\tau)$ is the correlation function, n is the frequency (in Hz), f is the dimensionless frequency and can be calculated as $f = nz/\overline{u}$ (z, measurement height above ground), u^* is the friction velocity, and the empirical constants A, B, C, δ , β , and γ vary based upon field site characteristics [see Tieleman (1992a), Teunissen (1980), Kaimal and Finnigan (1994), and Yu et al. (2008) for the values of the empirical constants used in calculations of Fig. 3d later]. Implementing the Taylor's frozen turbulence hypothesis, ε_{IDM} values were calculated using Eq. (6). In these calculations, the value of the Kolmogorov constant for the streamwise velocity component, $\alpha_u \approx 1/C_k$, was selected to be 0.52, and the value of $n^{5/3}S_u(n)$ was found from the average of the maximum and adjacent two points with 0.5-Hz intervals among the eight frequency bands from 0.5 to 4 Hz (Wyngaard and Coté 1971; Champagne et al. 1977; Oncley et al. 1996):

$$\varepsilon_{\text{IDM}} = \frac{2\pi}{\overline{u}} \left[\frac{n^{5/3} S_u(n)}{\alpha_u} \right]^{1.5}.$$
 (6)

Figure 3 shows the comparison of ε values calculated using both SSFM and IDM from our field experiments. As can be seen in this figure, $\varepsilon_{\rm SSFM}$ and $\varepsilon_{\rm IDM}$ values agree relatively well with the Pearson correlation coefficient squared (R^2) value of 0.92. Given the previously reported favorable performance of the SSFM in ε calculations for atmospheric surface-layer flows and its relatively less susceptibility to the turbulence intermittency (Muñoz-Esparza et al. 2018; Katul et al. 1994), we utilized ε values calculated using SSFM in this study and it was simply denoted as ε for the remainder of this paper. Using the calculated ε values, Kolmogorov length l_{η} and time τ_{η} scales for each of the subdatasets were estimated as follows:

$$l_{\eta} = \left(\frac{\vartheta^3}{\varepsilon}\right)^{1/4} \tau_{\eta} = \left(\frac{\vartheta}{\varepsilon}\right)^{1/2}.\tag{7}$$

Here, ϑ is the kinematic viscosity of air.

The surface-layer velocity spectra were also evaluated to elucidate the turbulence characteristics during in situ rainfall

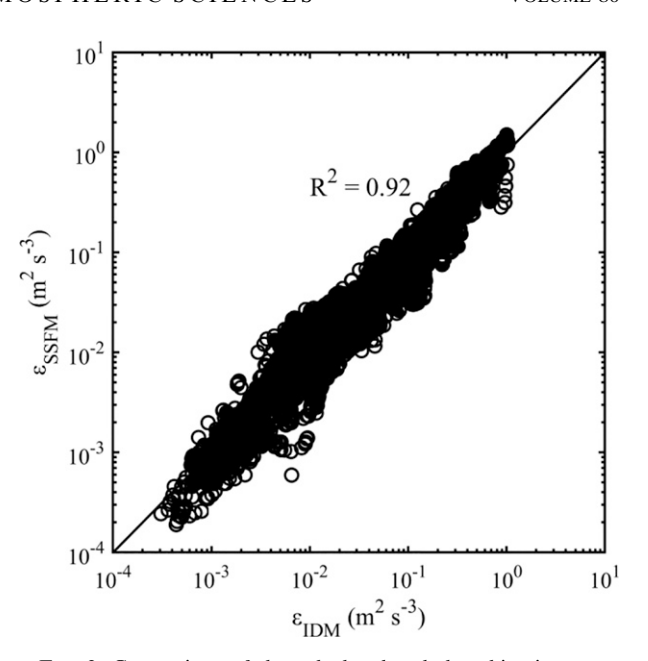


FIG. 3. Comparison of the calculated turbulent kinetic energy dissipation rate (ε) values using two different methods: second-order structure function method $\varepsilon_{\rm SSFM}$ and inertial dissipation range method $\varepsilon_{\rm IDM}$. Pearson correlation coefficient squared (R^2) value determined by linear regression was 0.92, indicating a good match between ε values calculated using the two methods.

measurements. Many of the previous studies considered isotropic turbulence (Wang and Maxey 1993; Squires and Eaton 1991; Aliseda et al. 2002; Stout et al. 1995; Fung 1998; Tom and Bragg 2019; Ireland et al. 2016; Good et al. 2014), although it should be noted that surface-layer turbulence can be isotropic in inertial scales, but it is not isotropic in large scales (Kaimal et al. 1972; Katul et al. 1995; Newsom et al. 2008; Darbieu et al. 2015; Liu et al. 2017; Brugger et al. 2018). Turbulence anisotropy in the surface layer was reported to be induced by thermal convection, thermal stratification, and wind shear (Liu et al. 2017; Brugger et al. 2018; Chamecki and Dias 2004). Isotropic turbulence velocity spectra in the inertial range follow the -5/3 power law and the ratio of the vertical (or lateral) to streamwise velocity spectra, $S_w(n)/S_u(n)$, is equal to 4/3 (Kaimal and Finnigan 1994; Piper and Lundquist 2004). Figure 4 presents various turbulence characteristics during our field observations. In Figs. 4a, 4b, and 4d, we considered two different periods with high ($u^* = 0.84 \,\mathrm{m \ s^{-1}}$) and low $(u^* = 0.33 \,\mathrm{m \ s^{-1}})$ wind shears that were recorded at 0100-0130 and at 0230-0500 UTC 25 May 2020, respectively, and in Fig. 4c, we considered the entire dataset to evaluate and compare the turbulence characteristics. In this study, u^* values were calculated using 30-min averaging time since the convergence time of u^* is larger than the 5-min averaging time used for calculating turbulence quantities from single variable time series (see Lenschow et al. 1994). Figure 4a shows the averaged velocity spectra of three velocity components for the selected two time periods. As can be seen in this figure, spectra for the streamwise and lateral velocity components indicate isotropic state (with slopes of -5/3) at larger

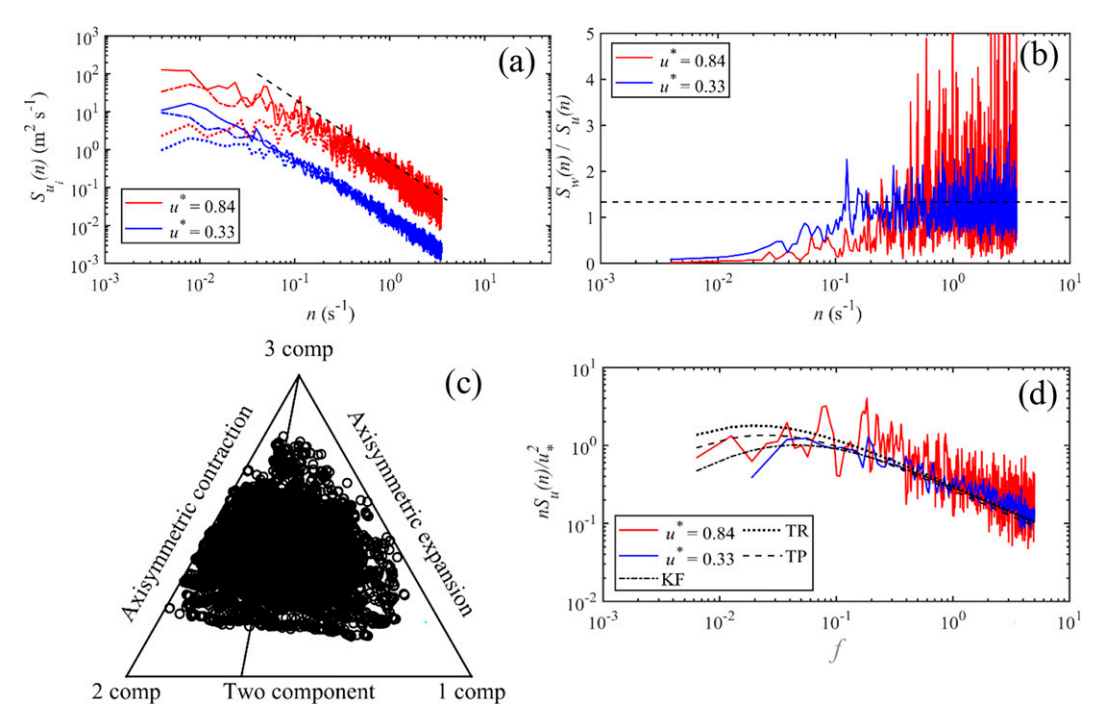


FIG. 4. Selected turbulence characteristics from our field observations. (a) Examples of velocity spectra of the three velocity components during high wind shear (friction velocity calculated using 30-min time averaging $u^* = 0.84 \,\mathrm{m \ s^{-1}}$: red lines; S_u : solid line; S_v : dash-dotted line; S_w : dotted line) and low wind shear ($u^* = 0.33 \,\mathrm{m \ s^{-1}}$: blue lines; S_u : solid line; S_v : dash-dotted line) with black dashed line indicating the 5/3 power law. (b) Examples of the ratio of vertical to streamwise velocity spectra $S_w(n)/S_u(n)$ during high (red) and low (blue) wind shear with the black horizontal dashed line denoting the 4/3 isotropy ratio. (c) Barycentric map that presents turbulence anisotropy for the entire wind observations (the top vertex denoted as "3 comp" indicates isotropy). (d) Example comparisons of the velocity spectra from high- and low-wind-shear conditions with the model spectra: KF = neutral Kansas model (dash-dotted line; Kaimal and Finnigan 1994), TR = Teunissen rural model (dotted line; Teunissen 1980), and TP = Tieleman perturbed terrain model (dashed line; Tieleman 1992a). Here, n is frequency (in s^{-1}) and f is nondimensional frequency.

scales than the one for the vertical velocity component as observed by Liu et al. (2017). During both of the time periods, the large scales do not exhibit isotropy. However, it is clear that isotropy was confined within smaller scales for the highwind-shear case than those of the low-wind-shear case. In Fig. 4b, $S_w(n)/S_u(n)$ values were compared with the 4/3 isotropy line. This figure indicates that turbulence was isotropic for n values around 1 Hz and larger for the high-wind-shear case and around 0.5 Hz and larger for the low-wind-shear case. In Fig. 4c, barycentric map proposed by Banerjee et al. (2007) is shown to illustrate the turbulence anisotropy level for each of the 5-min subdatasets in our entire dataset. The relevant calculation procedures are described in detail by Banerjee et al. (2007), Brugger et al. (2018), and Lumley (1979) and omitted here. According to this map, turbulence cannot be described as isotropic turbulence for any of the 5-min subdatasets, and most of the data are clustered toward axisymmetric contraction side, which qualitatively agrees with the findings of Brugger et al. (2018). In Fig. 4d, nondimensional form of the averaged velocity spectra as given in Eq. (5) are presented for the high- and low-wind-shear cases. In this figure, velocity spectra are compared with the neutral Kansas (KF) (Kaimal and Finnigan 1994), Teunissen rural (TR) (Teunissen 1980), and Tieleman perturbed (TP) (Tieleman 1992a) terrain models. It can be seen that KF and TP models fit the observed spectra well at the higher energy content. KF model predicted the observed normalized spectral density peak well for the low-wind-shear case, but predicted a lower peak value than the observations for the high-wind-shear case. Both TR and TP models predicted the peak-frequency locations at lower frequencies than the observed ones. Additional lowfrequency energy was observed in the spectra for the highwind-shear case. Similar observations were noted by Teunissen (1980) over rural terrain and by Tieleman (1992b) over heterogeneous terrain. Comparisons of the predictions by the three models and observed spectra indicate that the overall agreement between the KF model predictions and the observations is better, and the main differences are for the low-frequency end of the spectra for the high-wind-shear case. These differences may be related to the terrain roughness and memory of the upstream topography (Tieleman 1992a; Teunissen 1980; Panofsky et al. 1982).

The governing dimensionless parameters for this flow problem include Stokes number $[St_n, Eq. (8)]$, Froude number

TABLE 2. Turbulence characteristics of each rainfall event considered in this study. Table columns are \overline{U} : average streamwise velocity of the entire event; ε : average turbulent kinetic energy dissipation rate of the entire event; $\overline{\sigma_u}$ and $\overline{\sigma_w}$: average rms fluctuation velocities in streamwise and vertical directions, respectively, of the entire event; $\max(\overline{u_{3s}})$ and $\max(\overline{w_{3s}})$: maximum values of the 3-s-averaged gusts in streamwise and vertical directions, respectively, for the entire event; τ_{η} and τ_L : average Kolmogorov and integral time scales, respectively, of the entire event; $\overline{Re_{\lambda}}$: average and standard deviation of the Taylor Reynolds number of the entire event. Both upward (+) and downward (-) components of $\max(\overline{w_{3s}})$ are provided.

Event No.	\overline{U} (m s ⁻¹)	$\varepsilon (\mathrm{m^2 s^{-3}})$	$\overline{\sigma_u} \ (\text{m s}^{-1})$	$\overline{\sigma_w} \ (\text{m s}^{-1})$	$\max(\overline{u_{3s}}) \text{ (m s}^{-1})$	$\max(\overline{w_{3s}}) \ (\text{m s}^{-1})$	$\tau_{\eta}\left(\mathbf{s}\right)$	τ_L (s)	$\overline{\mathrm{Re}_{\lambda}}$
1	3.50	0.091	1.20	0.69	12.63	2.2; -1.8	0.025	6.78	4120 ± 1479
2	3.52	0.061	1.17	0.71	10.64	2.0; -1.9	0.025	7.93	4783 ± 1035
3	1.28	0.002	0.33	0.21	3.15	0.7; -0.7	0.097	10.63	1834 ± 489
4	2.28	0.028	0.83	0.50	8.46	1.2; -1.7	0.047	11.50	3429 ± 1548
5	2.73	0.097	1.16	0.70	7.64	1.5; -1.5	0.029	10.40	4196 ± 1312
6	5.73	0.115	1.73	1.01	13.63	2.0; -2.4	0.013	6.51	6112 ± 1072
7	0.45	0.021	0.38	0.24	2.74	0.7; -1.4	0.062	12.36	1017 ± 393
8	4.29	0.173	1.74	0.92	11.52	2.6; -2.0	0.013	10.97	5306 ± 733
9	2.09	0.015	0.62	0.37	4.86	1.3; -0.9	0.050	8.76	2286 ± 582
10	2.09	0.026	0.76	0.49	6.82	1.5; -1.5	0.038	6.56	2831 ± 883
11	5.26	0.338	2.02	1.13	13.40	2.5; -2.6	0.012	5.67	5167 ± 1043
12	3.04	0.058	1.17	0.68	7.50	2.4; -1.7	0.020	8.14	4051 ± 785
13	3.26	0.120	1.18	0.68	13.43	2.8; -2.5	0.026	9.47	3752 ± 2201
14	6.39	0.391	2.31	1.20	15.18	2.0; -1.8	0.008	3.90	5660 ± 1601
15	2.12	0.009	0.57	0.32	4.94	1.1; -1.0	0.043	8.69	2315 ± 1035
16	3.35	0.112	1.48	0.87	9.59	2.4; -2.3	0.012	6.11	4229 ± 593
17	2.23	0.025	0.73	0.48	6.56	1.4; -1.7	0.028	7.94	2575 ± 652

[Fr, Eq. (9)], particle and Taylor Reynolds numbers [Re_p and Re_{λ} , respectively, Eq. (10)]. Here, St_{η} and Re_{p} define the particle inertia relative to turbulence, and viscous forces, respectively, and Fr indicates the flow inertia relative to gravitational force, whereas the Re_{λ} provides the turbulence level that was encountered during the observations. In our analyses, Re_p is defined in terms of the vertical fall speeds of raindrops, V_f , and St_n is defined in terms of the particle relaxation time τ_p and Kolmogorov time scale τ_η , where τ_p for raindrops was calculated using the procedure described by Lovejoy and Schertzer (2008). The drag coefficient (C_D) values used in τ_D calculations [see Eq. (8)] were calculated using a polynomial fit to the laboratory data of Gunn and Kinzer (1949). The laboratory data are for the terminal fall of water drops with a range of diameters that encompasses raindrop diameters, and we fitted an eighth-degree polynomial function to the data in terms of D [see Eq. (11); D is in mm] to use it in C_D value predictions for the observed raindrops with the mean absolute relative error of 0.25% for 0.5 < D < 5.8 mm. Raindrop terminal fall speeds were calculated using the terminal speed parameterization by Atlas et al. (1973) [see Eq. (12)], where D is in mm and V_t is in m s⁻¹. There were no elevation corrections in our terminal speed calculations as the elevation effects on terminal speeds would be negligible for our field site that is only approximately 300 m above mean sea level:

$$St_{\eta} = \frac{\tau_p}{\tau_{\eta}}, \quad \tau_p = \left(\frac{\pi D \rho_w}{3C_D g \rho_a}\right)^{1/2}, \tag{8}$$

$$Fr = \frac{\varepsilon^{0.75}}{\vartheta^{0.25}g},\tag{9}$$

$$\operatorname{Re}_{p} = \frac{V_{f}D}{\vartheta}, \quad \operatorname{Re}_{\lambda} \approx \left(\frac{20\operatorname{Re}_{t}}{3}\right)^{0.5},$$
 (10)

$$C_D = 0.0003278D^8 - 0.0092D^7 + 0.1103D^6 - 0.7294D^5$$

 $+ 2.9114D^4 - 7.17D^3 + 10.6781D^2 - 8.9235D$
 $+ 3.8069,$ (11)

$$V_{t} = (9.65 - 10.3e^{-0.6D}). (12)$$

Here, ρ_a and ρ_w are air and water densities, respectively, and Re_t denotes the turbulent Reynolds number that is defined as Re_t = $k^2/\varepsilon\vartheta$.

Table 2 provides information on the relevant wind and turbulence characteristics of all of the rainfall events listed in Table 1. As can be seen from Tables 1 and 2, the rainfall events considered in this study covers wide parameter ranges for the relevant rainfall, wind, and turbulence parameters to elucidate the effects of wind and turbulence on the raindrop fall speeds.

4. Results and discussion

The results presented herein involve different parameters; hence, there are different data binning for these different parameters. Moreover, some of the figures include binning for multiple parameters. Therefore, bin selection procedure for the figures presented in this section is important and described as follows. Except for two later figures (Figs. 5 and 7), the results are presented by implementing two different binning for two different parameters. For those figures, binning was performed first for D using bin selections tabulated in Table 3, and then binning the data in each of the D bins by the

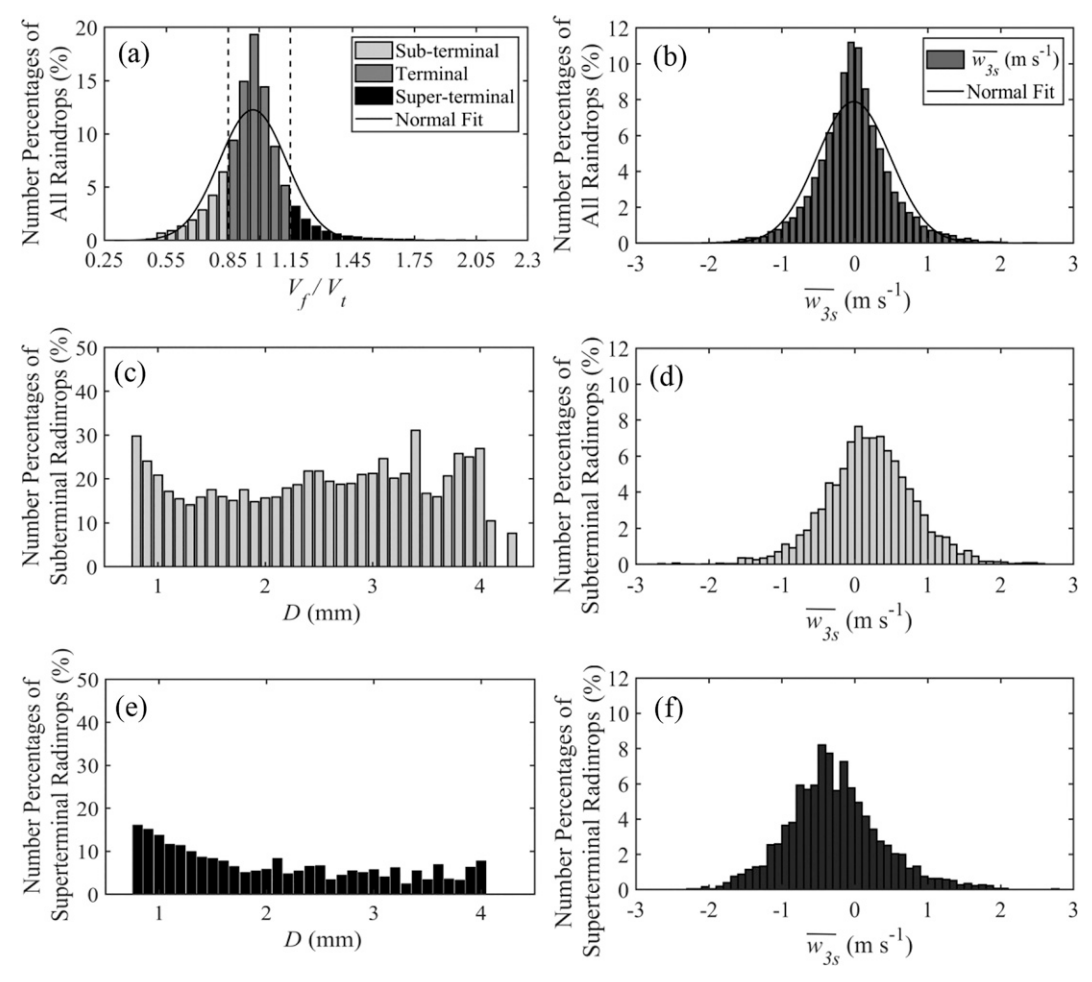


FIG. 5. Number percentages of all of the observed raindrops from the entire rainfall events distributed for raindrop fall classifications [i.e., (a),(c),(e) subterminal, terminal, and superterminal] and (b),(d),(f) exposure to 3-s-averaged vertical wind gust $(\overline{w_{3s}})$ values. (a) Percentages of raindrops distributed based upon scaled fall speed (V_f/V_t) spectrum with 0.05 as the bin width and the vertical dashed lines demarcating subterminal, terminal, and superterminal raindrop classifications. (c),(e) Percentages of (c) subterminal and (e) superterminal raindrops distributed over the observed raindrop diameter spectrum with 0.1-mm-diameter bin width. (b),(d),(f) Percentages of (b) all of the raindrops, (d) subterminal raindrops, and (f) superterminal raindrops distributed over the observed $\overline{w_{3s}}$ spectrum with 0.1 mm s⁻¹ as the bin width. Solid lines represent normal fit to the data for comparison purposes.

second parameter of interest (e.g., $\overline{u_{3s}}/\sigma_w$, σ_u/V_t , St_η). Bin selection for D included considerations for the value range and number of observations of the second parameters. In selecting the bin widths, we followed the quantitative procedure outlined by Freedman and Diaconis (1981), and increased the bin widths as necessary. Each of the bins presented in the figures covered at least 10 raindrops. This effort was to minimize the potential binning effects on our observational findings. Selected bin characteristics for different parameters are tabulated in Table 4. Later, histograms for a single parameter are presented using uniform bin widths and the selected bin widths for the parameters are specified in the figure caption (Fig. 5). Also later (Fig. 7), single parameter binning was implemented and selected bin characteristics are provided in Table 4. Note that, as tabulated in Table 4, binning characteristics for the same parameter in later figures (Figs. 7 and 9) differ due to the

abovementioned considerations for binning a single parameter (Fig. 7) and two parameters (Fig. 9).

In this study, sub- and superterminal raindrops are defined as raindrops with $V_f/V_t \le 0.85$ and $V_f/V_t \ge 1.15$, respectively, and raindrops with $0.85 < V_f/V_t < 1.15$ are considered as terminal raindrops. This raindrop classification criterion is stricter than the 30% cutoff value for the fall speed deviations from the predicted terminal speeds (i.e., $V_f/V_t \le 0.70$ for subterminal raindrops and $V_f/V_t \ge 1.30$ for superterminal raindrops) that was used by previous studies (e.g., Montero-Martínez et al. 2009). The 30% cutoff value was set in the previous studies mainly due to the uncertainty level in raindrop fall speed measurements in those studies. For the case of HOD measurements in this study, uncertainty of raindrop fall speed measurements is less than 10% for the raindrop sizes considered in this study (i.e., D > 0.75 mm), and the fall speed measurement

TABLE 3. Sub- and superterminal raindrop observations throughout the entire rainfall events. Table columns are D raindrop diameter bin; Sub and Super: percentages of the number of subterminal and superterminal raindrops among the entire raindrop population within each of the diameter bins; Sub/Super: ratio of the subterminal to superterminal raindrop numbers within each of the diameter bins; N: number raindrops within each of the diameter bins.

D (mm)	Sub (%)	Super (%)	Sub/Super	N
0.7–0.9	27.82	15.88	1.75	2890
0.9 - 1.1	20.74	13.36	1.55	4258
1.1-1.3	15.38	11.36	1.35	4409
1.3-1.5	15.53	8.52	1.82	3768
1.5 - 2.0	16.18	6.29	2.57	6377
2.0-2.5	18.18	6.30	2.88	3141
2.5-3.0	19.54	4.83	4.05	1346
3.0-6.5	21.26	4.46	4.76	762

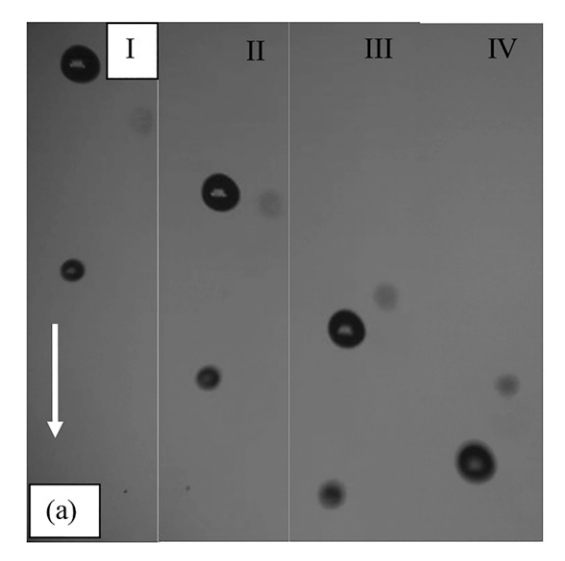
uncertainty decreases as raindrop size increases (Testik and Rahman 2016). Therefore, in the present study, in which we considered only raindrops that are larger than 0.75 mm in diameter, 15% cutoff value is adequate. Figure 5a presents percentages of total raindrops in each V_f/V_t bin for our entire dataset and compares the observed percentage distribution with a normal distribution fit. In this graph, raindrops are classified as subterminal, superterminal, and terminal based upon the specified criterion with 15% cutoff value. As can be seen, the number of subterminal raindrop observations (18.5% of the entire raindrop observations) was approximately twice that of

superterminal raindrop observations (9.5% of the entire raindrop observations). Sub- and superterminal raindrops exhibited a wide range of V_f/V_t values (i.e., $0.41 \le V_f/V_t \le 2.23$), indicating potential effects of turbulence and the wide range of turbulence scales on raindrop fall as discussed later in this section. Percentages of sub- and superterminal raindrops within each diameter bin are presented in Figs. 5c and 5e, respectively, and this information along with the total number of raindrops and ratio of the sub- and superterminal raindrop numbers for each diameter bin are tabulated in Table 3. Figure 5c shows that subterminal raindrops were present for all raindrop sizes (except in 4.2 mm diameter bin), and percentages of subterminal raindrops present in different size bins were rather uniform within a range of approximately 15%-30% (except for the largest two bins with small numbers of raindrops), showing no clear indication of diameter dependence. On the other hand, Fig. 5e shows that percentages of superterminal raindrops decrease as D increases up to around D = 2 mm and then become steady within a range of approximately 3%-7% for D > 2. Approximately 59% of the subterminal raindrops were smaller than 1.5 mm in diameter, whereas this was approximately 73% for the superterminal raindrops. The average and median diameters of all of the subterminal raindrops were 1.5 mm (with a standard deviation of 0.64 mm) and 1.34 mm, respectively, whereas the average and median diameters of all of the superterminal raindrops were 1.34 mm (with a standard deviation of 0.52 mm) and 1.2 mm, respectively. These observations indicate that the distributions of sub- and superterminal raindrops in the raindrop size spectrum are distinct, and different physical processes and

TABLE 4. Bin characteristics selected for the parameters and the relevant figures in this study. Bin width and number selection process is described in section 4.

σ_u/V_t^a (Fig. 7)	Re_{λ} (Fig. 8)	σ_{u-w}/V_t^a (Fig. 9)	St_{μ} (Fig. 10)	$\overline{u_{3s}}/\sigma_w$ (Fig. 12)
0-0.04	180-500	0-0.03	0–5	0-1.0
0.04-0.08	500-1000	0.03-0.06	5–10	1.0-2.0
0.08-0.12	1000-1500	0.06-0.09	10–15	2.0-3.0
0.12-0.16	1500-2000	0.09-0.12	15–20	3.0-4.0
0.16-0.2	2000-2500	0.12-0.15	20–25	4.0-5.0
0.2-0.24	2500-3000	0.15-0.2	25-30	5.0-6.0
0.24-0.28	3000-3500	0.2-0.25	30-40	6.0-7.0
0.28-0.32	3500-4000	0.25-0.3	40–50	7.0-8.0
0.32-0.36	4000-4500	0.3-0.35	50-75	8.0-9.0
0.36-0.4	4500-5000	0.35-0.4	75–100	9.0-10.0
0.4-0.44	5000-5500	0.4-0.5	100-150	10.0-25.0
0.44-0.48	5500-6000	0.5-0.65		
0.48-0.52	6000-6500	0.65-0.8		
0.52-0.56	6500-7000	0.8-1.0		
0.56-0.6	7000–7500			
0.6-0.64	7500-10 000			
0.64-0.68				
0.68-0.72				
0.72-0.76				
0.76-0.8				
0.8-0.84				
0.84-0.88				
0.88-1.04				

^a Different bin widths were used for σ_{tt}/V_t in Figs. 7 and 9 as raindrop diameter binning was also applied to the data in Fig. 9. First column is for σ_{tt}/V_t bin widths applied in Fig. 7, and third column is for σ_{tt}/V_t bin widths applied in Fig. 9.



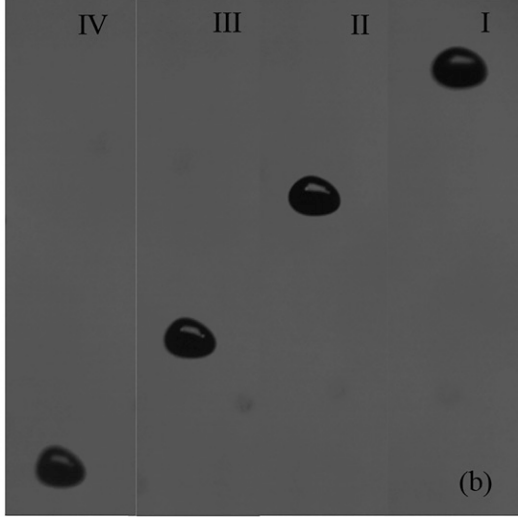


FIG. 6. Observed fall trajectories of large raindrops with superterminal fall speeds. (a) During positive (upward) 3-s vertical wind gust of $\overline{w_{3s}} = 1.084 \,\mathrm{m \ s^{-1}} : D = 3.03 \,\mathrm{mm}, \ V_f = 10.06 \,\mathrm{m \ s^{-1}}, \ V_h = 9.114 \,\mathrm{m \ s^{-1}}, \ \mathrm{and} \ V_t = 7.98 \,\mathrm{m \ s^{-1}}.$ (b) During negative (downward) 3-s vertical wind gust of $\overline{w_{3s}} = -0.696 \,\mathrm{m \ s^{-1}} : D = 4.04 \,\mathrm{mm}, \ V_f = 12.72 \,\mathrm{m \ s^{-1}}, \ V_h = -4.11 \,\mathrm{m \ s^{-1}}, \ \mathrm{and} \ V_t = 8.74 \,\mathrm{m \ s^{-1}}.$ Images (a) and (b) were constructed by augmenting 1-ms-apart sequential HOD images of the same raindrop side by side with the roman numerals embedded to indicate the increasing time sequence with increasing numbers, and the direction of gravity is shown by the downward-pointing arrow.

forcing are responsible for their occurrence. These factors affecting raindrop fall are discussed in the following subsections: vertical wind effects (section 4a), turbulence effects (section 4b), and wind shear effects (section 4c).

a. Vertical wind effects

It is expected that upward wind speeds would reduce raindrop fall speeds (i.e., headwind effects) and downward wind speeds would increase raindrop fall speeds (i.e., tailwind effects). To explore such potential effects of vertical wind speed on raindrop fall, Figs. 5b, 5d, and 5f show distributions of the 3-s-averaged vertical wind gust speed $(\overline{w_{3s}})$ for the entire raindrop dataset (Fig. 5b), for only the subterminal raindrops within the dataset (Fig. 5d), and for only the superterminal raindrops within the dataset (Fig. 5f), respectively. Here, we used 3-s averaging as gusts are typically measured in meteorological applications using a gust duration time of 3 s, which originated based upon response characteristics of earlier anemometers with response times of 2-5 s (Suomi and Vihma 2018). In calculating $\overline{w_{3s}}$ corresponding to an observed raindrop, the 3-s averaging window starts 3 s prior to HOD's observation of the raindrop. This was to represent the flow conditions that led to the observed raindrop response. Here, note that negative $\overline{w_{38}}$ values indicate that 3-s-averaged vertical wind gust at the observation instant was in the direction of gravity (i.e., tailwind conditions), and one would expect that it would affect the raindrop fall by increasing the fall speed (i.e., contributing toward a superterminal fall), and vice versa. As can be seen in Fig. 5b, the $\overline{w_{3s}}$ distribution for the entire raindrop dataset was similar to a Gaussian distribution with mean and standard deviation values of -0.015 and 0.51 m s⁻¹, respectively. The distribution of $\overline{w_{3s}}$ for the subterminal

raindrops (see Fig. 5d) is skewed toward positive $\overline{w_{3s}}$ values with the average $\overline{w_{3s}}$ value of 0.2 m s⁻¹, the standard deviation of 0.61 m s⁻¹, and skewness of -0.061. This observation is consistent with the aforementioned expected headwind effect of slowing down the raindrop fall. On the other hand, the distribution of $\overline{w_{3s}}$ for the superterminal raindrops (see Fig. 5f) is skewed toward negative $\overline{w_{3s}}$ values with the average $\overline{w_{3s}}$ value of -0.28 m s⁻¹, the standard deviation of 0.65 m s⁻¹, and skewness of 0.47. Similarly, this observation is consistent with the aforementioned expected tailwind effect of speeding up the raindrop fall. While having an impact on the sub- and superterminality of raindrops (more so for the superterminality of raindrops), $\overline{w_{3s}}$ alone is not sufficient to explain the sub- or superterminality of raindrop fall. If $\overline{w_{3s}}$ was the sole factor, we would have observed similar numbers of sub- and superterminal raindrops under the influence of the observed $\overline{w_{3s}}$ distribution presented in Fig. 5b, which was not the case for our raindrop observations.

Figure 6 shows the HOD images for the fall of large superterminal raindrops under positive (Fig. 6a) and negative (Fig. 6b) vertical wind speeds. As these raindrop observations exemplify, superterminal raindrops are not limited to only small raindrop sizes as previous observations indicated (Montero-Martínez et al. 2009; Montero-Martínez and García-García 2016; Larsen et al. 2014) and superterminal raindrops may be present even under high positive vertical winds ($\overline{w}_{3s} = 1.084 \,\mathrm{m \, s^{-1}}$ in Fig. 6a).

Figure 7 demonstrates the effects of vertical wind and turbulence on the sub- and superterminality of raindrop fall. Note that turbulence effects on raindrop fall are elaborated later in section 4b. In this figure, scaled raindrop fall speeds (V_f/V_t) for subterminal (Fig. 7a) and superterminal (Fig. 7c) raindrops and the scaled 3-s-averaged vertical wind gust

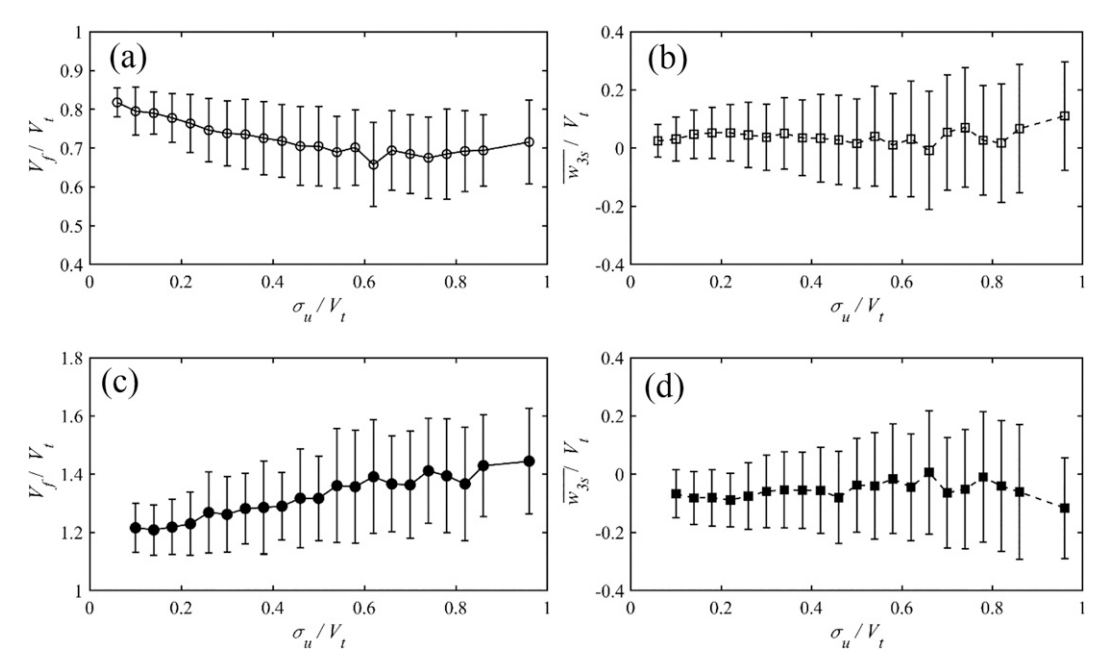


FIG. 7. (a),(c) Mean and standard deviations of V_f/V_t values for the observed (a) subterminal and (c) superterminal raindrops from all of the rainfall events as a function of σ_u/V_t . (b),(d) Mean and standard deviations of the 3-s-averaged vertical wind gust scaled by the predicted terminal fall speeds $\overline{w_{3s}}/V_t$ for the observed (b) subterminal and (d) superterminal raindrops from all of the rainfall events as a function of σ_u/V_t . Vertical bars represent standard deviations, open circles represent subterminal raindrops, and solid circles represent superterminal raindrops. Bin selections for σ_u/V_t is presented in Table 4.

speeds $(\overline{w_{3e}}/V_t)$ for subterminal (Fig. 7b) and superterminal (Fig. 7d) raindrops are presented as a function of the rootmean-square of the streamwise wind speed fluctuations scaled by the predicted terminal fall speeds (σ_u/V_t) . In this figure, mean and standard deviations of V_f/V_t values for both sub- and superterminal raindrops for each bin are shown with symbols (open circles—subterminal raindrops; and closed circles—superterminal raindrops) and vertical bars centered at the corresponding symbols, respectively. In Figs. 7a and 7c, the downward (upward) trend of subterminal (superterminal) raindrops with increasing σ_u/V_t values can be clearly seen. In Figs. 7b and 7d, mean and standard deviations of $\overline{w_{3s}}/V_t$, values for both sub- and superterminal raindrops for each bin are shown with symbols (open squares represent subterminal raindrops; and closed squares represent superterminal raindrops) and vertical bars centered at the corresponding symbols, respectively. As can be seen in Figs. 7b and 7d, mean $\overline{w_{3s}}/V$, values for all of the bins are positive for subterminal raindrops and negative for superterminal raindrops, indicating the potential presence of the aforementioned headwind and tailwind effects. Nevertheless, by comparing Fig. 7a with Fig. 7b and Fig. 7c with Fig. 7d and noting that abscissas of all of the graphs in Fig. 7 are identical, it can also be seen that mean $\overline{w_{3s}}/V_t$ values do not exhibit a trend in relation to the V_f/V_t values. Such a trend would be expected if headwind and tailwind effects were dominant over the effects of other processes in -determining the raindrop fall speed deviations. Indeed, if tailwind effects were dominant for the superterminal raindrops, one would expect to observe $\overline{w_{3s}}/V_t$ values to decrease for increasing V_f/V_t values, and if the

headwind effects were dominant for subterminal raindrops, one would expect to observe $\overline{w_{3s}}/V_t$ values to increase for decreasing V_f/V_t values. Nevertheless, the correlation coefficient values between V_f/V_t and $\overline{w_{3s}}/V_t$ values for both sub- and superterminal raindrops were 0.04 and 0.31, respectively, indicating that there is poor to no correlation between these two variables. Note that, for longer time intervals (i.e., 1 and 5 min), values of the correlation coefficient between raindrop fall speed and vertical airspeed were even smaller. On the other hand, Fig. 7 also shows that sub- and superterminality of raindrops increase with increasing σ_u/V_t values. These observations from Figs. 5 and 7 suggest that, in addition to D and $\overline{w_{3s}}$, there are parameters, for example, σ_u/V_t , that play a role in determining the raindrop fall speed deviations from the predicted terminal speeds.

b. Turbulence effects

Here, we discuss the turbulence effects on raindrop fall. The linkage between sub- and superterminal raindrop observations and rainfall rate has been noted previously (Montero-Martínez et al. 2009). Our observations (see Tables 1 and 2) show that the percentages of the sub- and superterminal raindrop occurrences appear to correlate better with Re_{λ} than rainfall rate. As an example, for the relation of the nonterminal fall of raindrops to \overline{R} and $\overline{Re_{\lambda}}$, events 5 and 14 in Tables 1 and 2 can be looked into. Here, \overline{R} and $\overline{Re_{\lambda}}$ denote the average rainfall rate and average Taylor Reynolds number for the entire rainfall event, respectively. In event 5, \overline{R} has the maximum value among the observed rainfall events with $\overline{R} = 18 \, \mathrm{mm \ h^{-1}}$,

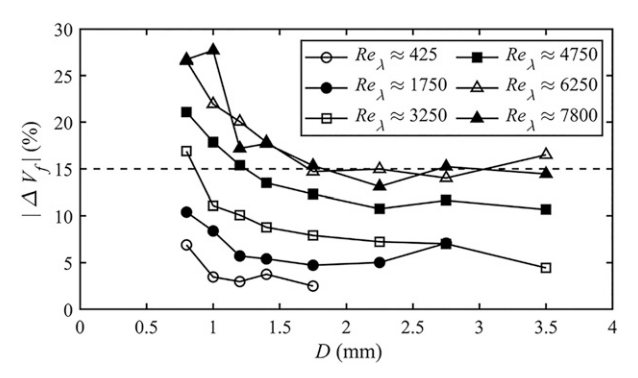


FIG. 8. Raindrop fall speed deviation percentages $|\Delta V_f|$ as a function of raindrop diameter D for different Re_λ values. Horizontal dashed line demarcates sub- and superterminal fall (above) and the terminal fall (below) based upon our 15% cutoff value fall classifications. Midbin values for Re_λ are provided in the legend, except for the smallest and largest Re_λ bins, for which mean Re_λ values are presented ($Re_\lambda \sim 425$ and 7800) due to the large differences between mean and mid values. Bin size selections are provided in Table 4, and only six bin sizes are shown in the figure for clarity purposes.

Re, value was 4196, and the occurrence percentages of sub- and superterminal raindrops were 14.1% and 3.6%, respectively. On the other hand, in event 14, \overline{R} value was 8.9 mm h⁻¹, \overline{Re}_{λ} value was approximately 5660, and the occurrence percentages of suband superterminal raindrops were 33.2% and 20.1%, respectively. For the 17 rainfall events tabulated in Tables 1 and 2, the correlation coefficient value between \overline{R} values and nonterminal raindrop percentages was 0.48, whereas the correlation coefficient value between Re, values and nonterminal raindrop percentages was 0.83. Therefore, we can conclude that Re_{λ} is a factor that determines the nonterminal fall of raindrops whereas R may weakly correlate with the nonterminal fall observations. Indeed, this weak correlation between R and the nonterminal fall observations may not have a physical foundation, except the potential effects of increased turbulence that may be driven by increasing rainfall rate. Instead, this weak correlation is likely due to the concurrent heavy wind and heavy rainfall events that are typical at our field site, which would lead us back to wind and turbulence effects in the nonterminal raindrop observations.

Figure 8 presents the effects of Re_{λ} and D on nonterminal fall of raindrops. In this figure, observations for both terminal

and nonterminal raindrops are presented, and the data are binned for both D and Re_{λ} with bin widths selected based on considerations for the data count in each bin and the distribution of the data counts across data ranges. Nonterminality of raindrops is represented by the average absolute values of the fall speed deviation percentages calculated as $|\Delta V_f| = 1/m \sum_{n=1}^{m} |V_{f_n} - V_{t_n}| / V_{t_n} \times 100$, where m is the number of raindrops in a given bin and n is the index that identifies the specific raindrops within that bin. Note that, in this representation of absolute values, there is no distinction between sub- and superterminality of raindrops. In the figure, the horizontal dashed line, which represents the 15% cutoff value for our terminal/nonterminal fall classifications, demarcates nonterminal (above) and terminal fall (below). As can be clearly seen in this figure, as Re_{\(\lambda\)} increases (see the figure legend), absolute fall speed deviation percentages increase across the raindrop size spectrum. Moreover, it is clear that smaller raindrops experience larger absolute fall speed deviation percentages than those of larger raindrops. A close look into the largest three Re_{λ} bins presented in Fig. 8 (Re_{λ} \approx 4750, 6250, and 7800) indicates that absolute fall speed deviation percentages become independent of Re_{λ} value (i.e., Re_{λ} similarity) for large Re_{\(\lambda\)} values (specifically indicated by the bins of $Re_{\lambda} \approx 6250$ and 7800). For such large Re_{λ} values, however, a significant percentage of the raindrops are nonterminal: i.e., for these largest three Re_{λ} bins ($Re_{\lambda} \ge 4750$), percentages of nonterminal raindrops in the smallest diameter bin of 0.8 mm range between 56% and 68%, and these nonterminal raindrop percentages decrease with increasing diameter bin to range between 27% and 49% in the largest diameter bin of 3.5 mm. To evaluate the statistical significance of the observed fall speed deviations during low- and high-turbulence conditions, t tests were conducted for the fall speed deviations for the lowest (~425) and highest (~7800) Re_{λ} bins. The null hypotheses were that there is no effect of Re_{λ} on the observed fall speed deviations. The t-test results are provided in Table 5. Note that, as can be seen in this table, there are very few raindrop observations in the three largest diameter bins of 2.25, 2.75, and 3.5 mm (i.e., two to five raindrops). As such, these diameter bins were not presented in Fig. 8; however, they were included in the t-test results presented in Table 5. These results indicate that observed fall speed deviations were statistically significant for all of the raindrop diameter bins (with caution for the largest three diameter bins with small sample sizes for

TABLE 5. Statistical *t*-test results for fall speed deviations ($|\Delta V_f|$) for different Re_{λ} values. Mean and standard deviation (std) values for $|\Delta V_f|$, and degrees of freedom (DoF) and *p* values are provided for Re_{λ} ≈ 425 and 7800.

	$Re_{\lambda} \approx 425$			<u> </u>			
D (mm)	Mean $ \Delta V_f $	Std $ \Delta V_f $	DoF	Mean $ \Delta V_f $	Std $ \Delta V_f $	DoF	p value
0.8	6.91	4.84	33	26.73	21.81	70	1.62×10^{-10}
1.0	3.47	2.72	39	27.70	21.11	74	3.24×10^{-15}
1.2	2.97	2.30	26	17.20	15.93	89	8.61×10^{-13}
1.4	3.75	1.25	11	17.70	13.09	61	1.17×10^{-11}
1.75	2.50	2.13	13	15.35	13.93	139	1.76×10^{-17}
2.25	0.88	0.73	5	13.12	11.25	82	2.42×10^{-15}
2.75	0.64	0.27	2	15.24	12.15	41	1.43×10^{-9}
3.5	0.85	0.33	2	14.46	11.83	46	5.17×10^{-10}

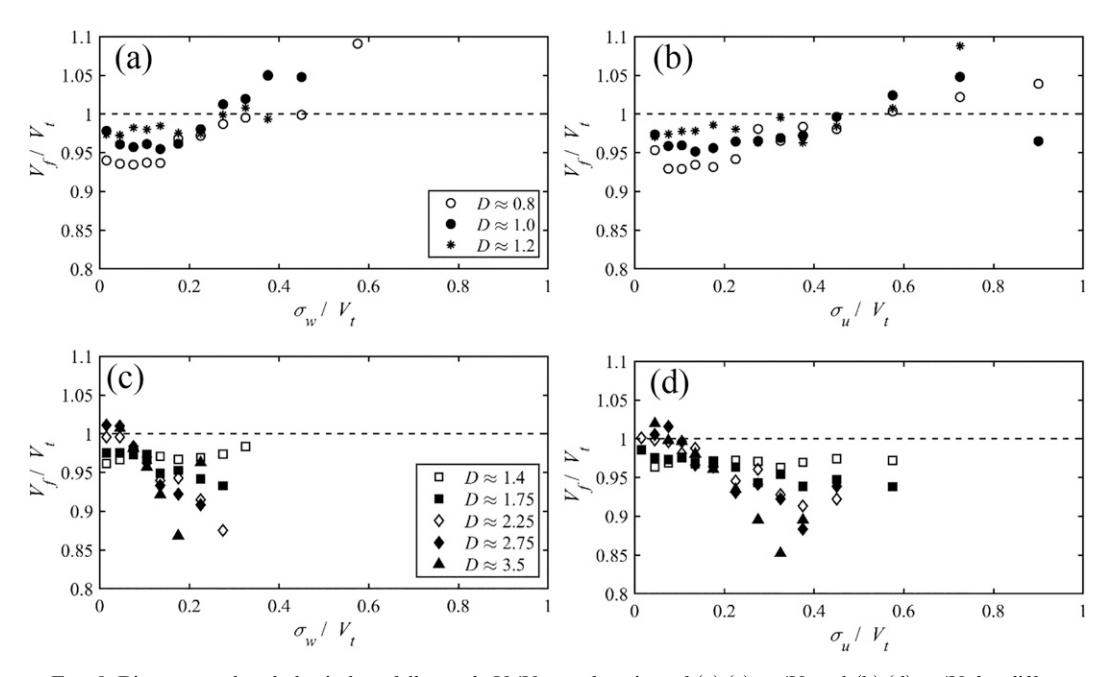


FIG. 9. Bin-averaged scaled raindrop fall speeds V_f/V_t as a function of (a),(c) σ_w/V_t and (b),(d) σ_u/V_t for different D values. Horizontal dashed line represents predicted terminal fall of raindrops. Midbin values for D (in mm) are provided in the legend, except for the largest diameter bin, for which mean D value is presented. Bin size selections for σ_w/V_t and σ_u/V_t are provided in Table 4.

 $Re_{\lambda} \approx 425$). Therefore, we can conclude that turbulence has a clear effect on raindrop fall speed.

Figure 9 is provided to further elucidate the turbulence effects on raindrop fall speed. In this figure, bin-averaged scaled raindrop fall speed (V_f/V_t) observations for different raindrop diameter bins (D) were provided as a function of σ_u/V_t (Figs. 9b,d) and σ_w/V_t (Figs. 9a,c). Due to large-scale anisotropy as noted above and the streamwise coordinate transformation, rms of only streamwise (σ_u/V_t) and vertical (σ_w/V_t) velocity components scaled by the predicted terminal fall speeds were used to represent the turbulence effects. Furthermore, since the raindrops are falling in the vertical direction, turbulence correlation is expected to be for a longer distance in the vertical direction than in the horizontal direction (Good et al. 2014). To plot this figure, the entire dataset was first binned by eight nonequidistant D bins, which are tabulated in Table 3. Then each D bin was binned for σ_u/V_t and σ_w/V_t bins, which are presented in Table 4. The bin widths for this figure were also chosen based upon considerations for the data count in each bin and the distribution of the data counts across data ranges. The entire raindrop dataset was divided into two categories as small (D < 1.3) and large ($D \ge 1.3$) raindrops. Note that the value of D = 1.3 mm for the categorization here was simply an approximation based upon the response of the raindrops to turbulence parameters observed in our study, which may be different under different conditions, and it is not a decisive value.

As can be seen in Fig. 9, the effect of turbulence on the fall behavior of small raindrops (Figs. 9a,b) is different than that of the large raindrops (Figs. 9c,d). For the case of small raindrops (D < 1.3), scaled raindrop fall speeds increase as σ_w/V_t

and σ_u/V_t values increase, and for relatively low σ_w/V_t and σ_{ν}/V_t values, these raindrops fall slower than their corresponding predicted terminal speeds $(V_f/V_t < 1)$. With increasing V_f/V_t values with increase in σ_w/V_t and σ_u/V_t values, raindrop fall speeds exhibit a transition from reduced $(V_f/V_t < 1)$ to enhanced $(V_t/V_t > 1)$ fall speeds. In a study by Kawanisi and Shiozaki (2008) on the turbulence effects on sediment settling speed, a similar transition from reduced to enhanced settling speeds was observed qualitatively. For the case of large raindrops ($D \ge 1.3$), observed fall speeds show a decreasing trend with increasing values of both σ_u/V_t and σ_w/V_t , except for $D \approx 1.4$ mm (Figs. 9c,d). This trend starts with fall speeds that are close to the corresponding predicted terminal speeds under relatively low turbulence levels (i.e., small σ_u/V_t and σ_w/V_t values in Figs. 9c,d), showing further evidence of turbulence effects on raindrop fall. Figures 9c and 9d clearly show also that as the raindrop sizes increase, fall speeds deviate further from the corresponding predicted terminal speeds. While the maximum average fall speed deviation for the selected diameter bins was observed to be approximately 15% (for $D \approx 3.5$ mm at $\sigma_u/V_t \approx 0.325$ in Fig. 9d), which may be perceived as barely subterminal considering the 15% threshold criterion used in this study, it should be noted that this is the average value of that specific bin, which includes subterminal, terminal, and superterminal raindrops. Therefore, these fall speed deviations, indeed, indicate significant presence of subterminal raindrops and their dominance in the averaging, which is further discussed later in this section. In a recent study by using direct numerical simulations (DNS), Ren et al. (2020) showed that water drops of 2 and 3 mm in diameter experienced turbulence-induced fall speed reductions. Their DNS results indicated that wake lengths of the drops were reduced in a turbulent ambient and that wake length reduction is significantly correlated to an increase in the drag coefficient of falling water drops, hence, a reduction in fall speeds. Although turbulence intensity values (<0.1) in Ren et al.'s study were much smaller than those in our study (average turbulence intensity value in our study was 0.399 with a standard deviation of 0.277), their numerical simulation findings for reduced fall speeds of water drops in a turbulent environment is consistent with our field observations for raindrops. Furthermore, Ren et al.'s simulations indicate larger fall speed reduction for 3 mm water drops than for 2 mm drops due to higher Re values of 3 mm drops. This is also consistent with our abovementioned finding for raindrops that fall speed reductions increase with increasing raindrop sizes as illustrated in Figs. 9c and 9d. Another important conclusion from Fig. 9 is that streamwise (σ_u/V_t) and vertical (σ_w/V_t) turbulence effects on the raindrop fall speed were similar. In a numerical study by using a stochastic model to simulate isotropic turbulence, Stout et al. (1995) noted greater than 35% reduction in water drop fall speed for $\sigma/V_t = 0.8$ and $Re_{p,0} = V_t D/v = 1000$. In our study, we observed that raindrops with $Re_{p,0} \approx 1000 \ (D \approx 2.25 \ mm)$ experienced 9% fall speed reduction $(V_t/V_t = 0.91)$ for $\sigma_u/V_t \approx 0.375$, which is in good agreement with Stout et al.'s finding of 10% fall speed reduction for $\sigma/V_t = 0.36$ and $\text{Re}_{p,0} \approx 1000$. Note that the fall speed response of even same-sized raindrops to the turbulent ambient may exhibit differences due to the turbulence properties such as intermittency and inhomogeneity as well as fall history of individual raindrops. Therefore, hereafter, we omitted the terminal raindrop observations from our analysis to more clearly demonstrate the relationships of raindrop sub- and superterminality with turbulence characteristics.

Figure 10 presents the relation between V_f/V_t and St_{η} for the observed sub- (Fig. 10b) and superterminal (Fig. 10a) raindrops, separately. This figure clearly shows that fall speed deviations from the predicted terminal speeds for both suband superterminal raindrops increase with increasing St_{η} values. Moreover, these deviations (i.e., fall speed reduction for subterminal raindrops and fall speed enhancement for superterminal raindrops) increase with decreasing raindrop size. This observed behavior is due to the relative importance of size-dependent particle inertia and turbulence level, as characterized by St_n, on raindrop fall. Montero-Martínez and García-García (2016) and Larsen et al. (2014), without turbulence considerations, also reported superterminal raindrops using different types of disdrometers. Nevertheless, our observations show differences than theirs. In particular, while Montero-Martínez and García-García (2016) and Larsen et al. (2014) reported superterminal raindrop fall for only small raindrops, our observations indicate that all raindrop sizes, small or large, may experience superterminal fall due to wind shear and turbulence effects (as shown in Fig. 10 for the turbulence effects). Figure 10a also shows that raindrop fall speed enhancement peaks with St_{η} . The peak (i.e., maximum superterminal fall speed for the corresponding size bin) occurs at a relatively small St_{η} value ($St_{\eta} \approx 35$) for the smallest raindrop size bin ($D \approx 0.8$ mm) and at increasingly larger St_n values as the raindrop size bins become larger. This finding suggests that the range of turbulent scales that affect the

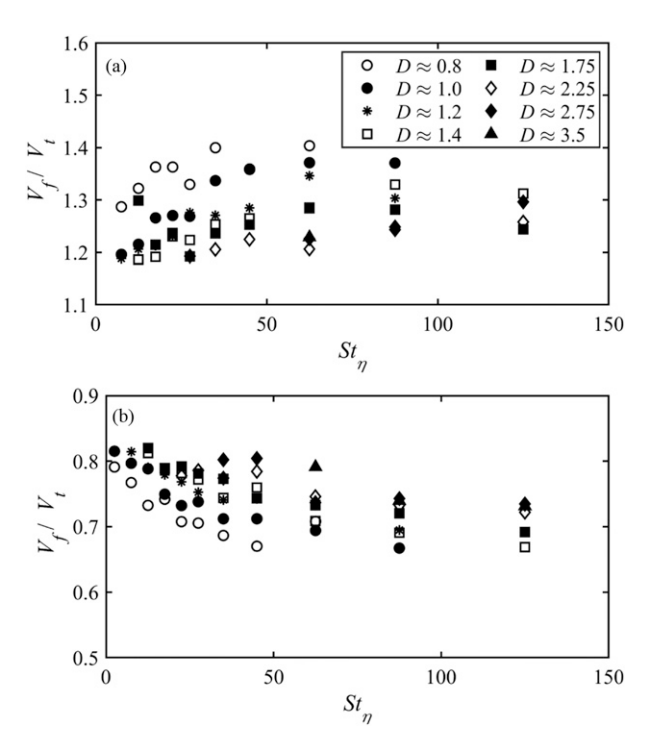


FIG. 10. Scaled raindrop fall speed V_f/V_t as a function of St_η for different D values for the observed (a) superterminal raindrops and (b) subterminal raindrops for the entire rainfall events. Midbin values for D (in mm) are provided in the legend, and bin size selections for St_η are provided in Table 4.

raindrop fall speed depends on the raindrop size. This is in qualitative agreement with the findings of Tom and Bragg (2019), where they also report that the range of turbulent scales responsible for the fall speed enhancement increases with increasing particle size. Our findings on the governing mechanism for the superterminal raindrop occurrences are discussed later in this section. However, for the physical mechanisms governing the subterminal raindrop occurrences, we can make an important remark from Fig. 10b. The increasing subterminality of the observed raindrops with decreasing raindrop diameter seen in this figure suggests that drag nonlinearity is not the sole mechanism, and there should be other mechanism(s) to explain the observed raindrop subterminality. Note that this is not to say that drag nonlinearity is not important as we can see from Table 3 that the ratio of the suband superterminal raindrop numbers increases with increasing raindrop size (from 1.75 for raindrops with $D \approx 0.8$ mm to 4.76 for raindrops with $D \approx 3.5$ mm). Other potential mechanisms that may cause raindrop subterminality include loitering and vortex trapping (see Nielsen 1993).

Figure 11 shows nine sequential HOD images that are 1 ms apart. In this figure, fall of four raindrops are presented in panels I–IX sequentially as an example. While the direction of gravity is vertical downward, there were significant horizontal movements of raindrops in and out of the camera focal plane as can be identified from transitions between sharp and blurry images of the same raindrops. These four raindrops

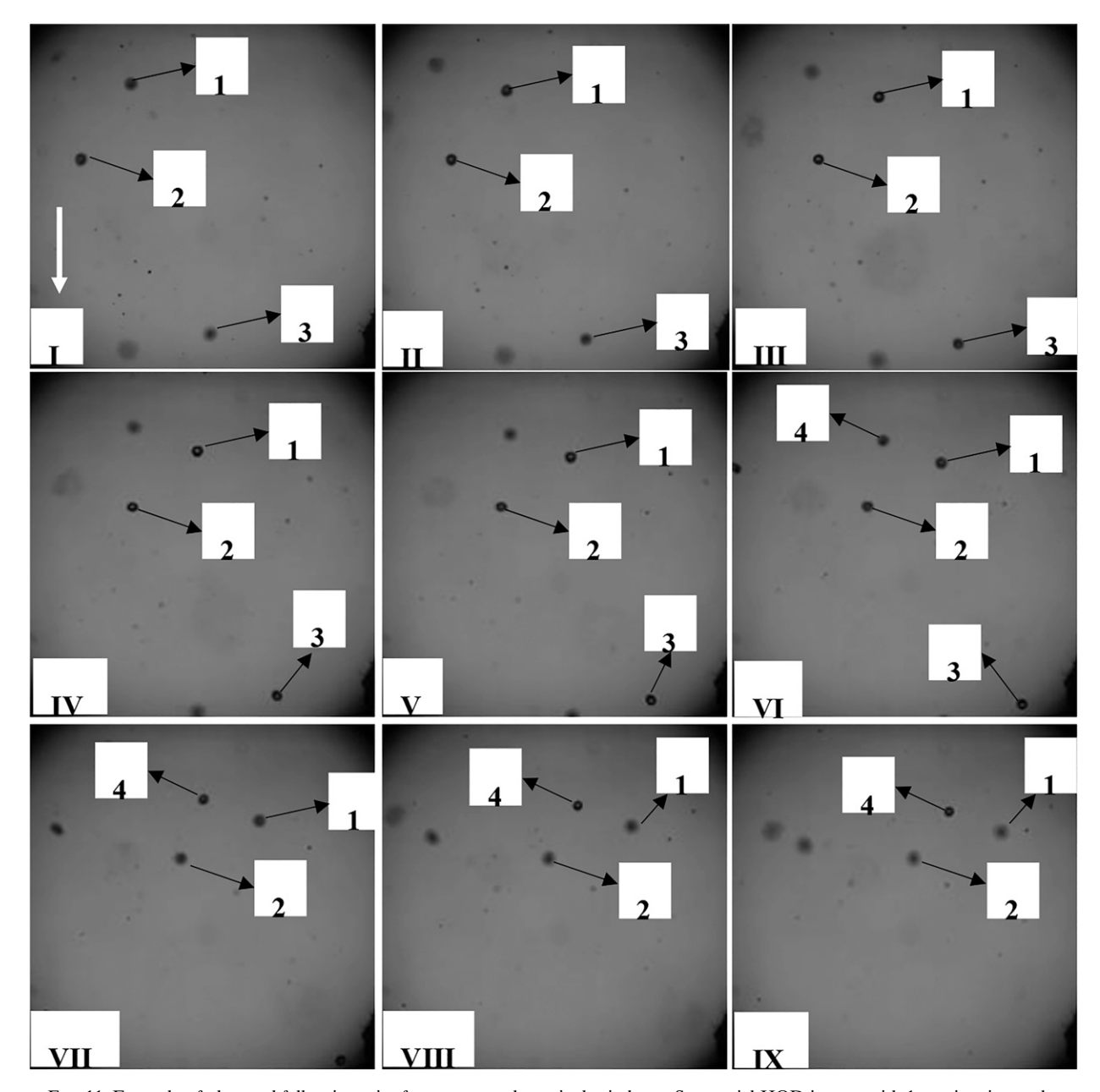


FIG. 11. Example of observed fall trajectories for extreme subterminal raindrops. Sequential HOD images with 1-ms time interval are marked with roman numerals in the time sequence and raindrops captured in these images are marked with Arabic numerals. Measured diameter D, fall speed V_f , and horizontal speed V_h of the observed raindrops (with the numbers in the subscripts indicating the raindrop numbers as marked in the images) are $D_1 = 2.25$ mm, $V_{f1} = 1.15$ m s⁻¹, and $V_{h1} = 4.24$ m s⁻¹; $D_2 = 1.95$ mm, $V_{f2} = -0.12$ m s⁻¹, and $V_{h2} = 3.29$ m s⁻¹; $D_3 = 1.91$ mm, $V_{f3} = 0.82$ m s⁻¹, and $V_{h3} = 4.27$ m s⁻¹; $D_4 = 1.91$ mm, $V_{f4} = 1.23$ m s⁻¹, and $V_{h4} = 4.34$ m s⁻¹. The white arrow pointing downward shows the direction of gravity.

(marked on each panel with numbers) were observed during event 11 (see Tables 1 and 2), and at the observation instant, $\mathrm{Re}_{\lambda} = 5647$, $\varepsilon = 0.564$ m² s⁻³, and $\overline{w_{3\mathrm{s}}} = -1.07\,\mathrm{m\,s^{-1}}$. Nevertheless, all four of the raindrops were observed to fall at extreme subterminal speeds ($V_f/V_t < 0.2$) at the observed instant. It is important here to note that the HOD software eliminated the raindrops in these images in the postprocessing stage as there were not enough sharp images of the same

raindrops (see Testik and Rahman 2016), and hence, these observations are not included in our analyses presented in this article. These raindrop fall behaviors were identified by visual inspections of the collected HOD images, and they are presented in Fig. 11 to provide an example of an extreme subterminal raindrop fall and discuss the potential governing physical mechanisms. In particular, raindrop 2 with D = 1.95 mm (measured from sharp images III–V) had a fall speed

of -0.12 m s^{-1} , which indicates that raindrop 2 was somewhat levitated with a minor vertical fall. This suggests that vortex trapping mechanism was not effective in this case because vortex trapping mechanism would result in raindrop fall speed that can be approximately estimated as the sum of the local vertical flow speed and the predicted terminal speed (Nielsen 1984). In this case, although the local flow velocity value in the vicinity of the raindrops is not available, it is highly unlikely that the vertical flow speed would be of similar magnitude to the predicted raindrop terminal speed of 6.45 m s⁻¹ when the measured $\overline{w_{3s}}$ was -1.07 m s^{-1} . Therefore, while a definitive conclusion on the governing physical mechanisms for the extreme subterminal fall of raindrops shown in Fig. 11 cannot be made in the absence of local flow velocity field observations in the raindrop vicinity, it is likely that loitering and/or drag nonlinearity is the responsible mechanism for the turbulence-induced subterminal raindrop fall.

c. Wind shear effects

In Fig. 12, we present the effects of wind shear on raindrop fall. Wind shear (S_h) is defined as $S_h = U/(z - d)$, where z (=10 m in our experiments) is the measurement elevation and d is the canopy height, which can be approximated as 5 m for the mean height of the trees surrounding our field site. Since z and d are constant in our case, we used the wind speed as the representative parameter for the wind shear effects. In our analysis, we used 3-s-averaged horizontal wind gust $(\overline{u_{3s}})$, instead of 5-min-averaged horizontal wind speed (U), as $\overline{u_{3s}}$ represents the horizontal wind speed that the raindrop experienced, and responded to, just before entering the HOD's measurement volume. In this figure, $\overline{u_{3s}}$ values were scaled by σ_w values to provide an indication of the relative importance of wind shear with respect to turbulence. Figure 12a presents V_f/V_t values for different diameter bins (shown with different symbols, see the legend) as a function of $\overline{u_{3e}}/\sigma_{uv}$ values for all of the nonterminal raindrops combined (i.e., sub- and superterminal raindrops combined). The data presented in this figure are binned for $\overline{u_{3s}}/\sigma_w$ (see Table 4), and V_f/V_t values are the average values for the corresponding $\overline{u_{3s}}/\sigma_w$ bins. It can be seen from this figure that as the $\overline{u_{3s}}/\sigma_w$ value increases the value of scaled raindrop fall speed, V_f/V_t , increases for all of the raindrop diameter bins. This clearly indicates that as the relative magnitude of wind shear becomes larger, raindrops favor a shift from turbulence-induced subterminal fall toward a superterminal fall. Figure 12b presents St_n values as a function of $\overline{u_{3s}}/\sigma_w$ values for all of the nonterminal raindrops combined. The data presented here are also binned for $\overline{u_{3s}}/\sigma_w$, and St_{η} values are the average values for the corresponding $\overline{u_{3s}}/\sigma_{w}$ bins. It can be seen in this figure that St_{η} values have a decreasing trend with increasing $\overline{u_{3s}}/\sigma_w$ values for the same raindrop diameter bins of Fig. 12a. Considering the formulations of St_{η} and τ_p in Eq. (8), a decrease in St_{η} value for a constant τ_p value would correspond to an increase in τ_η value (hence, a decrease in the ambient turbulence level). Therefore, the decreasing trend in St_n values with increasing $\overline{u_{3s}}/\sigma_w$ values seen in Fig. 12b is an indication of increasing τ_{η} values (hence, decreasing ambient turbulence levels) with increasing

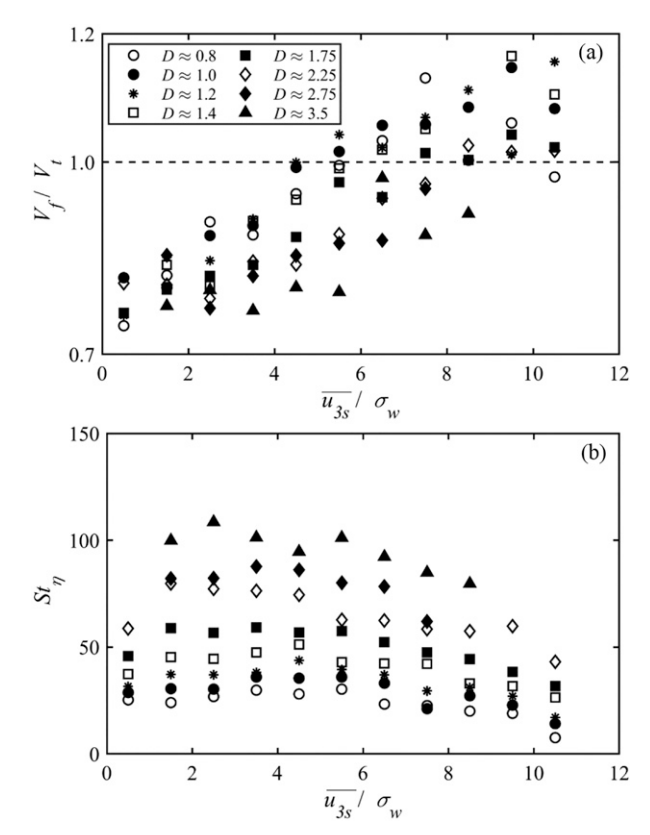


FIG. 12. (a) V_f/V_t and (b) St_η as a function of $\overline{u_{3\mathrm{s}}}/\sigma_w$ for all of the nonterminal raindrops combined for different raindrop diameters. Horizontal dashed line represents predicted terminal fall of raindrops. In the graphs, midbin values for $\overline{u_{3\mathrm{s}}}/\sigma_w$ are presented, except for the largest $\overline{u_{3\mathrm{s}}}/\sigma_w$ bin, for which mean of the $\overline{u_{3\mathrm{s}}}/\sigma_w$ values in this bin is used due to the large difference between the midbin and mean values. Midbin values for D (in mm) are provided in the legend, and bin size selections for $\overline{u_{3\mathrm{s}}}/\sigma_w$ are provided in Table 4.

 $\overline{u_{3s}}/\sigma_{w}$ values. As such, the trend in Fig. 12b further supports the increasing role of wind shear (represented by $\overline{u_{3s}}$) on raindrop fall as $\overline{u_{3s}}/\sigma_w$ values increase and implies that wind shear is responsible for the superterminal raindrop observations. The opposite is the case with decreasing $\overline{u_{3s}}/\sigma_w$ values, which supports that ambient turbulence is responsible for the subterminal raindrop observations as discussed earlier. From Fig. 12, it is clear that $\overline{u_{3s}}/\sigma_w$ is a useful parameter to assess the relative importance of turbulence and wind shear effects on raindrop fall speeds. To determine the statistical significance of this finding, we conducted t test for the deviations of V_f/V_t values with different $\overline{u_{3s}}/\sigma_w$ values. The null hypothesis was that there is no difference between the bin-averaged V_f/V_t values corresponding to different $\overline{u_{3s}}/\sigma_w$ bin values. The t tests were conducted for the same raindrop diameter bins at two different $\overline{u_{3s}}/\sigma_w$ bins: $\overline{u_{3s}}/\sigma_w = 0.5$ and $\overline{u_{3s}}/\sigma_w = 10.5$. These two $\overline{u_{3s}}/\sigma_w$ bins were selected as they correspond to high-turbulence-low-wind-shear $(\overline{u_{3s}}/\sigma_w = 0.5)$ and lowturbulence-high-wind-shear $(\overline{u_{3s}}/\sigma_w = 10.5)$ states. The *t*-test results are tabulated in Table 6. As can be seen in this table,

TABLE 6. Statistical <i>t</i> -test results for scaled fall speed (V_f/V_t) differences for different $\overline{u_{3s}}/\sigma_w$ values. Mean and standard deviation
(std) values for V_f/V_t , and degrees of freedom (DoF) and p values are provided for $\overline{u_{3c}}/\sigma_{vc} \approx 0.5$ and 10.5.

	$\overline{u_{3\mathrm{s}}}/\sigma_{_{W}} \approx 0.5$			ū			
D (mm)	Mean (V_f/V_t)	Std (V_f/V_t)	DoF	Mean (V_f/V_t)	Std (V_f/V_t)	DoF	p value
0.8	0.745	0.134	22	0.977	0.254	20	7.94×10^{-4}
1.0	0.820	0.203	39	1.083	0.233	28	6.42×10^{-6}
1.2	0.760	0.141	30	1.157	0.271	21	7.52×10^{-7}
1.4	0.765	0.077	25	1.106	0.254	9	2.39×10^{-3}
1.75	0.764	0.142	40	1.023	0.283	10	1.37×10^{-2}
2.25	0.811	0.122	14	1.018	0.241	14	7.58×10^{-3}
2.75	0.848	0.153	7	1.009	0.241	5	1.78×10^{-1}
3.5	0.791	0.022	3	0.755	0.000	0	_

the differences in V_f/V_t values at the two different turbulence wind shear states were statistically significant with a 95% confidence interval for all of the diameter bins, except for $D \sim 3.5$ mm. This finding presents an additional support to the abovementioned roles of wind shear and turbulence on the observed V_f/V_t deviations. The observed enhancement of raindrop fall speed induced by wind shear is likely caused by the behavior of the lift force acting on the raindrops. Several studies reported reversal of the lift force (i.e., from positive lift force acting vertically upward to negative lift force acting vertically downward in the direction of gravity) acting on spherical particles in shear flow with increasing Re_p values (Kurose and Komori 1999; Bagchi and Balachandar 2002; Hölzer and Sommerfeld 2009). In their DNS study for drag and lift forces acting on spherical water droplets in homogenous shear flows, Sugioka and Komori (2007) found that lift force reversal occurs for $Re_p \sim 50$ ($Re_p = 50$ corresponds to terminal raindrops with $D \sim 0.35$ mm). Although the droplet shape was spherical and Rep values ranged between 1 and $300 \text{ (Re}_p = 300 \text{ corresponds to terminal raindrops with}$ $D \sim 1.1$ mm) in their numerical study, the observed negative lift force (i.e., acting in the direction of gravity) is likely applicable for the case of raindrops under wind and responsible for the observed raindrop fall speed enhancement and superterminal raindrops under wind shear. Note that it is also possible that preferential sampling mechanism may have a role on the observed raindrop fall speed enhancement; however, an investigation on this would require a larger observational area that would enable observations for possible raindrop accumulations, which was not available in this study.

5. Summary and conclusions

In this study, we provide insights on the raindrop fall speed deviations from the predicted terminal fall speeds that have been observed by several recent studies (e.g., Testik et al. 2006; Montero-Martínez et al. 2009; Thurai et al. 2013; Larsen et al. 2014; Montero-Martínez and García-García 2016; Bringi et al. 2018; Bolek and Testik 2022). In particular, we elucidated the effects of wind and turbulence on the raindrop fall speeds, and revealed differing raindrop fall speed modulations induced by wind shear and turbulence. For our analyses, we utilized a unique dataset of HOD raindrop observations

that we collected during a wide range of wind, turbulence, and rainfall conditions over a 2-yr-long period. In total, our dataset included 26951 raindrop fall speed observations, 18.5% and 9.5% of which had sub- and superterminal fall speeds, respectively.

Our investigation showed that while the vertical component of the wind speed, represented by $\overline{w_{3s}}$ in our analysis, have an impact on the raindrop fall speed as one would expect, it was neither the sole nor the primary governing mechanism for the observed raindrop fall speed deviations from the predicted terminal speeds. Indeed, we found that, as Re, value increased, observed raindrop fall speed deviations distinctly increased for the entire raindrop diameter range of our study. This finding clearly demonstrated the presence of turbulence effects on raindrop fall speed. Our investigation on the turbulence effects on the raindrop fall speed showed that small (D < 1.3) and large $(D \ge 1.3)$ raindrops responded differently to turbulence. While fall speeds of the small raindrops transitioned from reduced to enhanced fall speeds with increasing values of σ_w/V_t and σ_u/V_t (i.e., average V_f/V_t values for σ_w/V_t and σ_u/V_t bins increased from ~0.92 to ~1.1; see Fig. 9), fall speeds of the large raindrops transitioned from near terminal to reduced fall speeds with increasing values of σ_w/V_t and σ_u/V_t (i.e., average V_t/V_t values for σ_w/V_t and σ_u/V_t bins decreased from \sim 1 to \sim 0.85; see Fig. 9). Therefore, we conclude that turbulence favors raindrop fall speed modifications toward superterminal fall of small raindrops and subterminal fall of large raindrops.

When considering only the observed sub- and superterminal raindrops and excluding the observed terminal raindrops, we found that small raindrops were more prone to wind shear and turbulence effects. This was evident by the differences of the observed fall speed deviations of different size raindrops as a function of St_η values. These findings can be considered as an indication of multiscale interactions between turbulence and raindrops. Moreover, we observed competing effects of wind shear and turbulence on raindrop fall. Our observations indicated that as the wind shear effects become more pronounced (i.e., increasing $\overline{u_{3s}}/\sigma_w$ values), raindrops favored increasing fall speeds toward a superterminal fall. On the contrary, raindrops favored decreasing fall speeds toward a subterminal fall as the turbulence effects become more pronounced (i.e., decreasing $\overline{u_{3s}}/\sigma_w$ values).

Our observations confirmed the presence of sub- and superterminal raindrops that have been reported in recent studies and showed that percentages of these raindrops are significant (28%) within the overall observed raindrop population. It is clear that wind shear and turbulence are the responsible physical mechanisms for the observed deviations of raindrop fall speeds from the predicted terminal fall speed values that are based upon the laboratory studies in the absence of ambient wind and turbulence. Therefore, terminal fall of raindrops based on such predictions should not be taken granted in relevant applications such as radar rainfall retrievals and calculations of the microphysical parameters such as rain rate and raindrop size distribution. In this study, our intention to restrict our analyses for raindrops with $D \ge 0.75$ mm was to cap HOD's measurement uncertainty level below approximately 10% for data quality purposes in our analyses and conclusions although HOD can observe raindrops as small as approximately 0.2-0.3 mm in diameter. Future field studies to further investigate the responsible physical mechanisms and to observe smaller raindrops (D < 0.75 mm) with smaller measurement uncertainty would benefit using a HOD unit with a higher-resolution camera and associated optics. Observations of smaller raindrops may provide further insights on the responsible physical mechanisms and processes as these raindrops are more prone to relevant forcings given their relatively small inertia. Furthermore, field investigations on competing contributions of wind shear and turbulence on raindrop fall may be complemented through controlled numerical [e.g., direct numerical simulations (DNS)] and laboratory (e.g., cloud chambers; see Shaw et al. 2020) experiments. Such controlled numerical and laboratory setups provide opportunities for well-characterized boundary and initial conditions and isolation of processes or mechanisms, among others. In light of our findings presented in this article and given the important applications of raindrop fall, the importance of future studies on this topic is evident.

Acknowledgments. This research was supported by the funds provided by the National Science Foundation under Grant AGS-1741250 to the first author (FYT). The second author is a graduate student under the guidance of FYT.

Data availability statement. Data presented in this article will be made available upon request from the corresponding author (Dr. Firat Y. Testik) and after completion of a fair use agreement.

APPENDIX

Nomenclature

C_D	Drag coefficient
C_k	Kolmogorov constant
d	Canopy height
D	Raindrop diameter
D_u	Streamwise second-order structure function
DSD	Raindrop size distribution
f	Dimensionless frequency

ND BOL	EK 1083
Fr	Froude number
g	Gravitational acceleration
HOD	High-speed optical disdrometer
k	Turbulent kinetic energy
KF	Kaimal and Finnigan (1994) spectra model
l_{u}	Integral length scale
l_{η}	Kolmogorov length scale
'n	Frequency
R	Rainfall rate
\overline{R}	Average rainfall rate for the entire rainfall event
R^2	Pearson correlation coefficient
Re_p	Particle Reynolds number using actual fall speed
$\operatorname{Re}_{p,0}$	Particle Reynolds number using terminal fall
* /	speed
R_u	Correlation function
Re_t	Turbulent Reynolds number
Re_{λ}	Taylor Reynolds number
$\overline{\text{Re}_{\lambda}}$	Average Taylor Reynolds number for the entire
	rainfall event
S_h	Wind shear
S_u	1D turbulent energy spectra of streamwise wind
	velocity
S_w	1D turbulent energy spectra of vertical wind
	velocity
St_{η}	Stokes number
T	Time lag
TP	Tieleman (1992a) perturbed terrain spectra model
TR	Teunissen (1980) rural spectra model
TRA	Total rain amount
и	Streamwise wind velocity
\overline{u}	Mean streamwise wind velocity
u'(t)	Fluctuation component of the streamwise wind
*	velocity
u*	Friction velocity
$\overline{u_{3\mathrm{s}}}$	3-s-averaged streamwise wind velocity
v	Lateral wind velocity
\overline{v}	Mean lateral wind velocity
v'(t)	Fluctuation component of the lateral wind velocity
V_{t}	Raindrop terminal fall speed
V_f	Raindrop observed fall speed
V_h	Raindrop horizontal velocity
w	Vertical wind velocity
\overline{w}	Mean vertical wind velocity
w'(t)	Fluctuation component of the vertical wind velocity
<u>w</u> -	3-s-averaged vertical wind velocity
w_{3s}	Measurement height
a_{η}	Kolmogorov acceleration scale
$\iota \iota_\eta$	Dissipation rate
	Dissipation rate found by the second-order
$\varepsilon_{ ext{SSFM}}$	structure function method
C	
$arepsilon_{ ext{IDM}}$	Dissipation rate found by the inertial differential method
σ	Average rms fluctuation velocity in streamwise
σ_u	direction

direction

direction

 σ_w

Average rms fluctuation velocity in vertical

- ρ_a Air density
- ρ_w Water density
- ρ_u Autocorrelation coefficient
- τ_u Integral time scale
- au_{η} Kolmogorov time scale
- τ_p Particle response time
- ζ Time separation
- θ Kinematic viscosity of air

REFERENCES

- Albertson, J. D., M. B. Parlange, G. Kiely, and W. E. Eichinger, 1997: The average dissipation rate of turbulent kinetic energy in the neutral and unstable atmospheric surface layer. *J. Geophys. Res.*, 102, 13423–13432, https://doi.org/10.1029/ 96JD03346.
- Aliseda, A., A. Cartellier, F. Hainaux, and J. C. Lasheras, 2002: Effect of preferential concentration on the settling velocity of heavy particles in homogeneous isotropic turbulence. *J. Fluid Mech.*, 468, 77–105, https://doi.org/10.1017/S0022112002001593.
- Atlas, D., R. C. Srivastava, and R. S. Sekhon, 1973: Doppler radar characteristics of precipitation at vertical incidence. Rev. Geophys., 11, 1–35, https://doi.org/10.1029/RG011i001p00001.
- Ayyalasomayajula, S., A. Gylfason, L. R. Collins, E. Bodenschatz, and Z. Warhaft, 2006: Lagrangian measurements of inertial particle accelerations in grid generated wind tunnel turbulence. *Phys. Rev. Lett.*, 97, 144507, https://doi.org/10.1103/ PhysRevLett.97.144507.
- Bagchi, P., and S. Balachandar, 2002: Effect of free rotation on the motion of a solid sphere in linear shear flow at moderate Re. *Phys. Fluids*, **14**, 2719–2737, https://doi.org/10.1063/1. 1487378.
- Banerjee, S., R. Krahl, F. Durst, and C. Zenger, 2007: Presentation of anisotropy properties of turbulence, invariants versus eigenvalue approaches. *J. Turbul.*, **8**, N32, https://doi.org/10.1080/14685240701506896.
- Bodini, N., J. K. Lundquist, and R. K. Newsom, 2018: Estimation of turbulence dissipation rate and its variability from sonic anemometer and wind Doppler lidar during the XPIA field campaign. Atmos. Meas. Tech., 11, 4291–4308, https://doi.org/ 10.5194/amt-11-4291-2018.
- —, —, R. Krishnamurthy, M. Pekour, L. K. Berg, and A. Choukulkar, 2019: Spatial and temporal variability of turbulence dissipation rate in complex terrain. *Atmos. Chem. Phys.*, 19, 4367–4382, https://doi.org/10.5194/acp-19-4367-2019.
- Bolek, A., and F. Y. Testik, 2022: Rainfall microphysics influenced by strong wind during a tornadic storm. *J. Hydrometeor.*, **23**, 733–746, https://doi.org/10.1175/JHM-D-21-0004.1.
- Bringi, V., M. Thurai, and D. Baumgardner, 2018: Raindrop fall velocities from an optical array probe and 2-D video disdrometer. *Atmos. Meas. Tech.*, 11, 1377–1384, https://doi.org/ 10.5194/amt-11-1377-2018.
- Brugger, P., G. G. Katul, F. De Roo, K. Kröniger, E. Rotenberg, S. Rohatyn, and M. Mauder, 2018: Scalewise invariant analysis of the anisotropic Reynolds stress tensor for atmospheric surface layer and canopy sublayer turbulent flows. *Phys. Rev. Fluids*, 3, 054608, https://doi.org/10.1103/PhysRevFluids. 3.054608.
- Chamecki, M., and N. L. Dias, 2004: The local isotropy hypothesis and the turbulent kinetic energy dissipation rate in the atmospheric surface layer. *Quart. J. Roy. Meteor. Soc.*, **130**, 2733–2752, https://doi.org/10.1256/qj.03.155.

- Champagne, F. H., C. A. Friehe, J. C. LaRue, and J. C. Wynagaard, 1997: Flux measurements, flux estimation techniques, and fine-scale turbulence measurements in the unstable surface layer over land. J. Atmos. Sci., 34, 515–530, https://doi.org/10. 1175/1520-0469(1977)034<0515:FMFETA>2.0.CO;2.
- Chatterjee, C., F. Porcù, S. Das, and A. Bracci, 2022: An investigation on super- and sub-terminal drops in two different rain categories and climate regimes. *Remote Sens.*, 14, 2515, https://doi.org/10.3390/rs14112515.
- Chen, X., Z. Liu, Y. Chen, and H. Wang, 2020: Analytical expression for predicting the reduced settling velocity of small particles in turbulence. *Environ. Fluid Mech.*, 20, 905–922, https://doi.org/10.1007/s10652-019-09731-8.
- Darbieu, C., and Coauthors, 2015: Turbulence vertical structure of the boundary layer during the afternoon transition. *Atmos. Chem. Phys.*, 15, 10 071–10 086, https://doi.org/10.5194/acp-15-10071-2015.
- Das, S. K., S. Simon, Y. K. Kolte, U. V. M. Krishna, S. M. Deshpande, and A. Hazra, 2020: Investigation of raindrops fall velocity during different monsoon seasons over the Western Ghats, India. *Earth Space Sci.*, 7, e2019EA000956, https://doi.org/10.1029/2019EA000956.
- Davidson, P. A., 2015: Turbulence: An Introduction for Scientists and Engineers. 2nd ed. Oxford University Press, 630 pp.
- Foken, T., and C. J. Napo, 2008: Micrometeorology. Springer, 306 pp. Freedman, D., and P. Diaconis, 1981: On the histogram as a density estimator: L2 theory. Z. Wahrscheinlichkeitstheorie Verw. Geb., 57, 453–476, https://doi.org/10.1007/BF01025868.
- Fung, J. C. H., 1993: Gravitational settling of particles and bubbles in homogeneous turbulence. J. Geophys. Res., 98, 20287– 20297, https://doi.org/10.1029/93JC01845.
- —, 1998: Effect of nonlinear drag on the settling velocity of particles in homogeneous isotropic turbulence. *J. Geophys. Res.*, 103, 27905–27917, https://doi.org/10.1029/98JC02822.
- Garrett, T. J., and S. E. Yuter, 2014: Observed influence of riming, temperature, and turbulence on the fallspeed of solid precipitation. *Geophys. Res. Lett.*, 41, 6515–6522, https://doi.org/10.1002/2014GL061016.
- Good, G. H., P. J. Ireland, G. P. Bewley, E. Bodenschatz, L. R. Collins, and Z. Warhaft, 2014: Settling regimes of inertial particles in isotropic turbulence. *J. Fluid Mech.*, 759, R3, https://doi.org/10.1017/jfm.2014.602.
- Gunn, R., and G. D. Kinzer, 1949: The terminal velocity of fall for water droplets in stagnant air. *J. Meteor.*, 6, 243–248, https://doi.org/10.1175/1520-0469(1949)006<0243:TTVOFF> 2.0.CO:2.
- Higgins, C. W., G. G. Katul, M. Froidevaux, V. Simeonov, and M. B. Parlange, 2013: Are atmospheric surface layer flows ergodic? *Geophys. Res. Lett.*, 40, 3342–3346, https://doi.org/10. 1002/grl.50642.
- Højstrup, J., 1981: A simple model for the adjustment of velocity spectra in unstable conditions downstream of an abrupt change in roughness and heat flux. *Bound.-Layer Meteor.*, 21, 341–356, https://doi.org/10.1007/BF00119278.
- Hölzer, A., and M. Sommerfeld, 2009: Lattice Boltzmann simulations to determine drag, lift and torque acting on non-spherical particles. *Comput. Fluids*, 38, 572–589, https://doi.org/10.1016/j.compfluid.2008.06.001.
- Ireland, P. J., A. D. Bragg, and L. R. Collins, 2016: The effect of Reynolds number on inertial particle dynamics in isotropic turbulence. Part 2. Simulations with gravitational effects. *J. Fluid Mech.*, 796, 659–711, https://doi.org/10.1017/jfm.2016.227.

- Jabbari, A., A. Rouhi, and L. Boegman, 2016: Evaluation of the structure function method to compute turbulent dissipation within boundary layers using numerical simulations. J. Geophys. Res. Oceans, 121, 5888–5897, https://doi.org/10.1002/ 2015JC011608.
- Kaimal, J. C., and J. J. Finnigan, 1994: Atmospheric Boundary Layer Flows: Their Structure and Measurement. Oxford University Press, 289 pp.
- —, J. C. Wyngaard, Y. Izumi, and O. R. Coté, 1972: Spectral characteristics of surface-layer turbulence. *Quart. J. Roy. Meteor. Soc.*, 98, 563–589, https://doi.org/10.1002/qj.49709841707.
- Katul, G. G., M. B. Parlange, and C. R. Chu, 1994: Intermittency, local isotropy, and non-Gaussian statistics in atmospheric surface layer turbulence. *Phys. Fluids*, 6, 2480–2492, https://doi. org/10.1063/1.868196.
- —, —, J. D. Albertson, and C. R. Chu, 1995: Local isotropy and anisotropy in the sheared and heated atmospheric surface layer. *Bound.-Layer Meteor.*, 72, 123–148, https://doi.org/ 10.1007/BF00712392.
- Kawanisi, K., and R. Shiozaki, 2008: Turbulent effects on the settling velocity of suspended sediment. J. Hydraul. Eng., 134, 261–266, https://doi.org/10.1061/(ASCE)0733-9429(2008)134: 2(261).
- Kurose, R., and S. Komori, 1999: Drag and lift forces on a rotating sphere in a linear shear flow. J. Fluid Mech., 384, 183–206, https://doi.org/10.1017/S0022112099004164.
- Larsen, M. L., A. B. Kostinski, and A. R. Jameson, 2014: Further evidence for superterminal raindrops. *Geophys. Res. Lett.*, 41, 6914–6918, https://doi.org/10.1002/2014GL061397.
- Lenschow, D. H., J. Mann, and L. Kristensen, 1994: How long is long enough when measuring fluxes and other turbulence statistics? *J. Atmos. Oceanic Technol.*, **11**, 661–673, https://doi.org/10.1175/1520-0426(1994)011<0661:HLILEW>2.0.CO;2.
- Liu, H., R. Yuan, J. Mei, J. Sun, Q. Liu, and Y. Wang, 2017: Scale properties of anisotropic and isotropic turbulence in the urban surface layer. *Bound.-Layer Meteor.*, 165, 277–294, https://doi. org/10.1007/s10546-017-0272-z.
- Lovejoy, S., and D. Schertzer, 2008: Turbulence, raindrops and the *l*^{1/2} number density law. *New J. Phys.*, **10**, 075017, https://doi.org/10.1088/1367-2630/10/7/075017.
- Lumley, J. L., 1979: Computational modeling of turbulent flows. Adv. Appl. Mech., 18, 123–176, https://doi.org/10.1016/S0065-2156(08)70266-7.
- Maxey, M. R., 1987: The gravitational settling of aerosol particles in homogeneous turbulence and random flow fields. *J. Fluid Mech.*, 174, 441–465, https://doi.org/10.1017/S0022112087000193.
- —, and S. Corrsin, 1986: Gravitational settling of aerosol particles in randomly oriented cellular flow fields. *J. Atmos. Sci.*, 43, 1112–1134, https://doi.org/10.1175/1520-0469(1986)043 <1112:GSOAPI>2.0.CO;2.
- Montero-Martínez, G., and F. García-García, 2016: On the behaviour of raindrop fall speed due to wind. *Quart. J. Roy. Meteor. Soc.*, **142**, 2013–2020, https://doi.org/10.1002/qj.2794.
- —, A. B. Kostinski, R. A. Shaw, and F. García-García, 2009: Do all raindrops fall at terminal speed? *Geophys. Res. Lett.*, 36. L11818. https://doi.org/10.1029/2008GL037111.
- Muñoz-Esparza, D., R. D. Sharman, and J. K. Lundquist, 2018: Turbulence dissipation rate in the atmospheric boundary layer: Observations and WRF mesoscale modeling during the XPIA field campaign. *Mon. Wea. Rev.*, 146, 351–371, https://doi.org/10.1175/MWR-D-17-0186.1.

- Murray, S. P., 1970: Settling velocities and vertical diffusion of particles in turbulent water. J. Geophys. Res., 75, 1647–1654, https://doi.org/10.1029/JC075i009p01647.
- Nemes, A., T. Dasari, J. Hong, M. Guala, and F. Coletti, 2017: Snowflakes in the atmospheric surface layer: Observation of particle-turbulence dynamics. *J. Fluid Mech.*, 814, 592–613, https://doi.org/10.1017/jfm.2017.13.
- Newsom, R., R. Calhoun, D. Ligon, and J. Allwine, 2008: Linearly organized turbulence structures observed over a suburban area by dual-Doppler lidar. *Bound.-Layer Meteor.*, 127, 111– 130, https://doi.org/10.1007/s10546-007-9243-0.
- Nielsen, P., 1984: On the motion of suspended sand particles. J. Geophys. Res., 89, 616–626, https://doi.org/10.1029/JC089iC01p00616.
- —, 1993: Turbulence effects on the settling of suspended particles. J. Sediment. Res., 63, 835–838, https://doi.org/10.1306/D4267C1C-2B26-11D7-8648000102C1865D.
- Nieuwstadt, F. T. M., and P. G. Duynkerke, 1996: Turbulence in the atmospheric boundary layer. Atmos. Res., 40, 111–142, https://doi.org/10.1016/0169-8095(95)00034-8.
- Niu, S., X. Jia, J. Sang, X. Liu, C. Lu, and Y. Liu, 2010: Distributions of raindrop sizes and fall velocities in a semiarid plateau climate: Convective versus stratiform rains. J. Appl. Meteor. Climatol., 49, 632–645, https://doi.org/10.1175/2009JAMC2208.1.
- Oncley, S. P., C. A. Friehe, J. C. Larue, J. A. Businger, E. C. Itsweire, and S. S. Chang, 1996: Surface-layer fluxes, profiles, and turbulence measurements over uniform terrain under nearneutral conditions. *J. Atmos. Sci.*, 53, 1029–1044, https://doi.org/10.1175/1520-0469(1996)053<1029:SLFPAT>2.0.CO;2.
- Panofsky, H. A., D. Larko, R. Lipschutz, G. Stone, E. F. Bradley, A. J. Bowen, and J. Højstrup, 1982: Spectra of velocity components over complex terrain. *Quart. J. Roy. Meteor. Soc.*, 108, 215–230, https://doi.org/10.1002/qj.49710845513.
- Pei, B., F. Y. Testik, and M. Gebremichael, 2014: Impacts of raindrop fall velocity and axis ratio errors on dual-polarization radar rainfall estimation. *J. Hydrometeor.*, 15, 1849–1861, https://doi.org/ 10.1175/JHM-D-13-0201.1.
- Piper, M., and J. K. Lundquist, 2004: Surface layer turbulence measurements during a frontal passage. J. Atmos. Sci., 61, 1768–1780, https://doi.org/10.1175/1520-0469(2004)061<1768: SLTMDA>2.0.CO;2.
- Rahman, K., and F. Y. Testik, 2020: Shapes and fall speeds of freezing and frozen raindrops. J. Hydrometeor., 21, 1311– 1331, https://doi.org/10.1175/JHM-D-19-0204.1.
- Ren, W., J. Reutzsch, and B. Weigand, 2020: Direct numerical simulation of water droplets in turbulent flow. *Fluids*, 5, 158, https://doi.org/10.3390/fluids5030158.
- Rosa, B., and J. Pozorski, 2017: Impact of subgrid fluid turbulence on inertial particles subject to gravity. J. Turbul., 18, 634–652, https://doi.org/10.1080/14685248.2017.1317099.
- Shaw, R. A., and Coauthors, 2020: Cloud–aerosol–turbulence interactions: Science priorities and concepts for a large-scale laboratory facility. *Bull. Amer. Meteor. Soc.*, 101, E1026–E1035, https://doi.org/10.1175/BAMS-D-20-0009.1.
- Squires, K. D., and J. K. Eaton, 1991: Preferential concentration of particles by turbulence. *Phys. Fluids*, A3, 1169–1178, https://doi.org/10.1063/1.858045.
- Stout, J. E., S. P. Arya, and E. L. Genikhovich, 1995: The effect of nonlinear drag on the motion and settling velocity of heavy particles. *J. Atmos. Sci.*, 52, 3836–3848, https://doi.org/ 10.1175/1520-0469(1995)052<3836:TEONDO>2.0.CO;2.
- Sugioka, K.-I., and S. Komori, 2007: Drag and lift forces acting on a spherical water droplet in homogeneous linear shear air

- flow. J. Fluid Mech., **570**, 155–175, https://doi.org/10.1017/S0022112006003065.
- Suomi, I., and T. Vihma, 2018: Wind gust measurement techniques—From traditional anemometry to new possibilities. Sensors, 18, 1300, https://doi.org/10.3390/s18041300.
- Testik, F. Y., and A. P. Barros, 2007: Toward elucidating the microstructure of warm rainfall: A survey. Rev. Geophys., 45, RG2003, https://doi.org/10.1029/2005RG000182.
- —, and M. Gebremichael, 2010: Rainfall: State of the Science. Amer. Geophys. Union, 287 pp.
- —, and M. K. Rahman, 2016: High-speed optical disdrometer for rainfall microphysical observations. *J. Atmos. Oceanic Technol.*, 33, 231–243, https://doi.org/10.1175/JTECH-D-15-0098.1.
- —, A. P. Barros, and L. F. Bliven, 2006: Field observations of multimode raindrop oscillations by high-speed imaging. *J. At*mos. Sci., 63, 2663–2668, https://doi.org/10.1175/JAS3773.1.
- Teunissen, H. W., 1980: Structure of mean winds and turbulence in the planetary boundary layer over rural terrain. *Bound.-Layer Meteor.*, **19**, 187–221, https://doi.org/10.1007/BF00117220.
- Thurai, M., V. N. Bringi, W. A. Petersen, and P. N. Gatlin, 2013: Drop shapes and fall speeds in rain: Two contrasting examples. J. Appl. Meteor. Climatol., 52, 2567–2581, https://doi.org/10.1175/JAMC-D-12-085.1.
- Tieleman, H. W., 1992a: Universality of velocity spectra. 11th Australasian Fluid Mechanics Conf., Hobart, Australia, University of Tasmania, 965–968, https://www.afms.org.au/proceedings/11/Tieleman_1992.pdf.

- —, 1992b: Wind characteristics in the surface layer over heterogeneous terrain. J. Wind Eng. Ind. Aerodyn., 41, 329–340, https://doi.org/10.1016/0167-6105(92)90427-C.
- Tom, J., and A. D. Bragg, 2019: Multiscale preferential sweeping of particles settling in turbulence. *J. Fluid Mech.*, 871, 244–270, https://doi.org/10.1017/jfm.2019.337.
- Vickers, D., and L. Mahrt, 1997: Quality control and flux sampling problems for tower and aircraft data. J. Atmos. Oceanic Technol., 14, 512–526, https://doi.org/10.1175/1520-0426(1997)014 <0512:QCAFSP>2.0.CO;2.
- Wang, L.-P., and M. R. Maxey, 1993: Settling velocity and concentration distribution of heavy particles in homogeneous isotropic turbulence. *J. Fluid Mech.*, 256, 27–68, https://doi.org/10.1017/S0022112093002708.
- Wilczak, J. M., S. P. Oncley, and S. A. Stage, 2001: Sonic anemometer tilt correction algorithms. *Bound.-Layer Meteor.*, 99, 127–150, https://doi.org/10.1023/A:1018966204465.
- Wyngaard, J. C., and O. R. Coté, 1971: The budgets of turbulent kinetic energy and temperature variance in the atmospheric surface layer. *J. Atmos. Sci.*, **28**, 190–201, https://doi.org/10.1175/1520-0469(1971)028<0190:TBOTKE>2.0.CO;2.
- Yang, T. S., and S. S. Shy, 2003: The settling velocity of heavy particles in an aqueous near-isotropic turbulence. *Phys. Flu*ids, 15, 868–880, https://doi.org/10.1063/1.1557526.
- Yu, B., A. Gan Chowdhury, and F. J. Masters, 2008: Hurricane wind power spectra, cospectra, and integral length scales. *Bound.-Layer Meteor.*, 129, 411–430, https://doi.org/10.1007/ s10546-008-9316-8.

Copyright of Journal of the Atmospheric Sciences is the property of American Meteorological Society and its content may not be copied or emailed to multiple sites or posted to a listserv without the copyright holder's express written permission. However, users may print, download, or email articles for individual use.